International Journal of Heat and Mass Transfer 217 (2023) 124644

Contents lists available at ScienceDirect

International Journal of Heat and Mass Transfer

journal homepage: www.elsevier.com/locate/ijhmt

A coupled level-set and volume-of-fluid (CLSVOF) method for prediction of microgravity flow boiling with low inlet subcooling on the international space station

Issam Mudawar *, Sunjae Kim, Jeongmin Lee

Purdue University Boiling and Two-Phase Flow Laboratory (PU-BTPFL) School of Mechanical Engineering, Purdue University, 585 Purdue Mall, West Lafayette, IN 47907, USA

ARTICLE INFO

Keywords:
Flow boiling
Microgravity
International space station (ISS)
Coupled level-set and volume-of-fluid (CLSVOF)

ABSTRACT

The present study is part of a series of NASA-supported investigations of flow boiling of n-perfluorohexane (n-PFH, C_6F_{14}) under microgravity on the International Space Station (ISS). The fluid physics and heat transfer characteristics of flow boiling with low inlet subcooling are explored using the Flow Boiling and Condensation Experiment (FBCE) (which is actual name of the test facility), the largest endeavor in microgravity two-phase research conducted to date. Experimental data are collected from the FBCE's Flow Boiling Module (FBM), which features a rectangular channel with 5.0-mm x 2.5-mm cross-section and 114.6-mm heated length. Results for three flow rates are used to explore the effects of mass velocity on flow structure and heat transfer characteristics in the absence of the body force. A Computational Fluid Dynamics (CFD) model is constructed to predict the measured FBM results. The CFD model employs the Coupled Level-Set and Volume-of-Fluid (CLSVOF) method, which is modified with improved interface capture and additional force terms in the momentum equation to determine the bubble dynamics more accurately. Validity of the CFD model is assessed in two ways, by comparing predictions against video-captured interfacial behavior and heat transfer data. The CFD model shows good ability to capture detailed evolution of the interfacial structure both across and along the flow channel, including bubble nucleation, growth, departure, and coalescence, as well as axial development of dominant flow patterns. Details of the flow structure are examined via axial development of both flow velocity and void fraction profiles. Similarly, heat transfer results are presented in terms of streamwise variations of both wall temperature and fluid temperature, which are also predicted accurately with the CFD model. Overall, this study proves the CFD model is an effective method for both design and performance assessment of flow boiling subsystems in space vehicles.

1. Introduction

1.1. Two-phase thermal management and its challenge for upcoming space missions

The utilization of space for a multitude of functions, such as electronic correspondence, global communications, scientific inquiry, and national security, has ushered in a new era of competition in the realm of space exploration. Space is viewed as the next common global resource, comparable to the oceans and cyberspace, which has prompted both public and private sectors to invest competitively in future space ventures.

The increased scope, magnitude, intricacy, and duration of space missions have resulted in commensurate increases in both electrical power requirements and heat dissipation. To ensure the success of these missions, it is imperative to minimize the weight and size of all thermal management subsystems while effectively tackling the high levels of heat removal.

One particularly noteworthy example of these subsystems is the profusion of high performance electronic and power devices incorporated into spacecraft and planetary habitats, both Lunar and Martian. These devices and their associated subsystems are projected to generate increased levels of heat, thereby necessitating the implementation of more effective thermal management strategies, to ensure reliability and prevent any potential malfunctions, while being mindful of the

* Corresponding author.
E-mail address: mudawar@ecn.purdue.edu (I. Mudawar).
URL: https://engineering.purdue.edu/BTPFL (I. Mudawar).

https://doi.org/10.1016/j.ijheatmasstransfer.2023.124644
Received 27 May 2023; Received in revised form 15 August 2023; Accepted 23 August 2023
Available online 6 September 2023

Nomenclature

A_c	cross-sectional area of channel (mm^2)
Bo	Boiling number, (q''/Gh_{fg})
c	cell size (mm)
C_D	bubble drag coefficient
C_L	coefficient in Eq. (20)
d_b	bubble diameter (mm)
E	energy per unit mass (J/kg)
G	mass velocity (kg/m^2 s)
H	longer dimension of channel's cross section (mm)
h	enthalpy (J/kg K)
h_{fg}	latent heat of vaporization (J/kg K)
H_{tc}	distance between thermocouple bead and wetted surface of copper slab (mm)
I	turbulence intensity
K	proportionality constant
k_{eff}	effective thermal conductivity (W/m K)
k_s	thermal conductivity of copper slab (W/m K)
L_a	adiabatic length of flow channel in experiment (mm)
L_d	development length of flow channel in experiment (mm)
L_e	exit length of flow channel in experiment (mm)
$L_{entrance}$	adiabatic entry length in computational domain (mm)
L_{exit}	adiabatic exit length in computational domain (mm)
L_h	heated length of flow channel (mm)
$\dot{m}$	mass flow rate (kg/s)
P	pressure (Pa)
P_h	heated perimeter of channel (=2 W) (mm)
q''	heat flux, total electrical power input divided by wetted area ($2WL_h$) of heating wall (W/m^2)
r_c	mass transfer intensity factor for condensation
Re	Reynolds number
r_e	mass transfer intensity factor for evaporation
S_c	bubble collision dispersion force term (N/m^2)
S_D	drag force term (N/m^2)
S_E	source term in energy equation (W/m^2)
S_M	source term in momentum equation (N/m^2)
S_{sl}	shear-lift force term (N/m^2)
S_{st}	surface tension force term (N/m^2)
T	temperature (°C, K)
ΔT_w	wall superheat (°C, K)
t	time (s)
u	velocity (m/s)
u'	turbulent fluctuating component of velocity (m/s)
u_r	velocity difference between liquid and vapor (m/s)
u_t	liquid fluctuation velocity due to bubble agitation (m/s)
W	shorter dimension of channel's cross section (mm)
x	coordinate in computational domain (mm)
x_e	thermodynamic equilibrium quality
y	coordinate in computational domain (mm)
y^+	dimensionless distance perpendicular to channel walls
z	axial coordinate in computational domain (mm)

Greek symbols

α	volume of fraction; void fraction
α_{max}	dense packing limit
θ	contact angle (°)
κ	curvature
μ	dynamic viscosity (kg/m s)
ρ	density (kg/m^3)
σ	surface tension (N/m)
φ	level-set function
ψ	ratio of average heat flux to single phase heat flux based on heated surface area

Subscripts

b	bubble
c	condensation
e	evaporation
f	liquid
g	vapor
in	inlet
m	mixture
out	outlet
sat	saturation
sp	single phase
sub	subcooling
tc	thermocouple
w	heated wall
z	axial location

Acronyms

BCD	bubble collision dispersion
CFD	computational fluid dynamics
CLSVOF	coupled level-set and volume-of-fluid method
CHF	critical heat flux
CSF	continuous surface force
FBCE	flow boiling and condensation experiment
FBM	flow boiling module
FDB	fully developed boiling
FIR	fluid integrated rack
ISS	international space station
LS	level-set method
nPFH	n-Perfluorohexane
NVG	net vapor generation
ONB	onset of nucleate boiling
PDB	partially developed boiling
PU-BTPFL	Purdue university boiling and two-phase flow laboratory
SST	shear-stress transport
UDF	user-defined function
VOF	volume-of-fluid method

paramount importance of compact and lightweight design. Overall, conventional thermal management approaches using single-phase liquid cooling are inadequate for fulfilling these objectives, as they exhibit comparatively low heat transfer coefficients. In contrast, the utilization of both sensible and latent heat of the coolant in two-phase thermal management can significantly improve heat transfer, increasing heat transfer coefficients by one to two orders of magnitude, compared to single-phase counterparts. This renders two-phase thermal management especially well-suited for systems where high heat fluxes must be dissipated while maintaining the compactness and lightweight goals of the cooling system. Therefore, a thorough understanding of two-phase fluid physics is of paramount importance to the development of thermal management solutions. This is true not only for electronic and power devices, but also a broad range of space-related applications, such as nuclear fission/Rankine power cycles for forthcoming space missions to the Moon, Mars, and deep space, vapor compression heat pumps for future Lunar and Martian habitats, the implement of cryogenic fluids in nuclear thermal propulsion systems, and the establishment of cryogenic fuel depots in space.

Key to proper operation of a two-phase cooling system in reduced gravity is ability to tackle the effects of diminished buoyancy, which is the product of density difference between liquid and vapor and gravity,

and whose magnitude can have a profound influence on the motion of vapor relative to the liquid. For example, in Earth gravity, the component of buoyancy-induced body force perpendicular to a heated wall aids in detaching of bubbles away from the wall, thereby delaying the onset of insulating vapor layer formation, a precursor to Critical Heat Flux (CHF), which is known to trigger an uncontrolled increase in wall temperature at high heat fluxes. For microgravity, with the absence of buoyancy, interfacial dynamics are governed by surface tension and flow inertia, which collectively regulate all aspects of flow boiling along a heated channel. The absence of buoyancy can increase the probability of vapor bubble coalescence into partial or continuous vapor blankets, thus increasing the likelihood for CHF to occur at comparatively low heat fluxes. CHF, a phenomenon that results in severe degradation in heat transfer coefficient due to the loss of liquid access to the heating surface, can be highly dependent on the prevailing gravity. In scenarios involving heat-flux-controlled surfaces, CHF may trigger an unsteady and uncontrollable escalation in surface temperature, leading to material degradation, such as melting, burning, or other irreversible damages. Consequently, CHF is regarded as the most crucial design and safety parameter for most terrestrial and space applications involving flow boiling with heat-flux-controlled surfaces.

Apart from the imperative to reduce weight and volume and address high heat fluxes, the choice of cooling strategy for space applications is heavily contingent on the type of cooling hardware deployed. Two-phase heat transfer can be achieved by variety of cooling schemes, including boiling in capillary flows, pool boiling, falling films, flow boiling in macro-channels, flow boiling in mini/micro-channels, jet impingement, sprays, and hybrid cooling schemes. These schemes are effective at enhancing heat transfer performance by capitalizing upon a coolant's both latent and sensible heat. These studies formed a foundation for recent efforts at Purdue University Boiling and Two-Phase Laboratory (PU-BTPFL) centered on selecting the most suitable and relevant thermal management schemes for adoption in space applications. Key takeaways for each scheme in microgravity applications are as follows [1]:

(i) Despite their passive circulation attributes, capillary devices (e.g., heat pipes, capillary pumped loops, loop heat pipes) can only tackle very small power densities.
(ii) Pool boiling (e.g., using thermosyphons) is very problematic in microgravity since the absence of a body force to remove bubbles from the heated surface causes the produced vapor to aggregate into a few enormously sized bubbles that resist liquid replenishment and therefore culminate in unusually low CHF.
(iii) Falling-film schemes, because of reliance on gravity to drive the cooling liquid film, are inoperable in microgravity.
(iv) Macro-channel and mini/micro-channel boiling are well suited to cooling high-heat-flux surfaces in space applications. Key to their adaptability are small weight and volume requirements (often using "cold plates") and ability to tackle high-heat-fluxes, the latter being an outcome of reliance on fluid motion rather than body force to flush bubbles away from, and sustain supply of bulk liquid to the heated surface. Notably, flow boiling in rectangular flow channel is the primary focus for the present study.
(v) While jet impingement is well known for ability to tackle very high heat flux situations, to maintain uniform surface temperatures for temperature-sensitive devices, they demand use of multiple jets, thereby greatly increasing coolant flow rate requirements, which is undesirable in space applications.
(vi) Spray cooling mirrors the high flux advantages of jets but, by breaking the liquid flow into fine droplets that are dispersed upon the heating surface, provides better cooling uniformity with lesser flow rate than jets. This is one reason sprays are found in several space applications especially in fuel delivery and chill-down. On the other hand, spray cooling is less desirable in cold plates because they require a relatively large orifice-to-surface distance to ensure liquid breakup into droplet, which increases the size and weight of cooling hardware beyond what is normally acceptable in space thermal management systems.

However, some pose challenges to implementation in real-life thermal management systems. For example, capillary flows are known to provide comparatively limited heat transfer performance, pool boiling and falling films require gravity to sustain operation, and jets and sprays demand high flow rates. Among the different schemes, the most common cooling hardware adopted for spacecraft avionics are cold plates, which are aluminum modules having the form of hollow plates. These plates contain a single coolant inlet and outlet, and feature rectangular flow passages wherein the coolant circulates, while the electronic or power devices are mounted on one of the outer surfaces. A comprehensive thermal management system may consist of several cold plates that are connected to a main cooling loop in various series/parallel arrangements. Therefore, channel flow boiling is considered the foremost candidate for thermal management of avionics in space applications and, as such, is the primary focus of the present study.

1.2. Development of two-phase flow models

Accurate modeling of interfaces is crucial for predicting the local fluid flow structure and macro-scale flow boiling regime in two-phase flow simulations, which serve as a foundation for heat transfer predictions for such flows. Three primary methods are used for computing two-phase flow, namely the (i) *interface fitting method*, (ii) *interface tracking method*, and (iii) *interface capturing method* [2]. The interface fitting method employs a moving mesh technique to represent a sharp phase interface, but it has limitations in handling bubble coalescence and breakup. Additionally, modifying the grids to follow a transient moving interface requires significant computational resources, which poses a considerable challenge for design purposes. The interface tracking method is a hybrid Eulerian–Lagrangian mesh technique that reconstructs and re-meshes grids in real-time to continuously track deforming interfaces. This method is highly accurate, as it can align the interface right onto the surface of a mesh cell, thereby mitigating numerical diffusion and oscillation issues at the interface. However, the computational cost of the interface tracking method is also substantial. The interface capturing method is an Eulerian-based approach that employs an indicator function to detect the position of moving interfaces on a fixed grid. It is a cost-effective and versatile method for computing two-phase flows and effectively captures topological changes in bubble structure, including coalescence and breakup. For this reason, this method is widely used in computational investigations of two-phase problems.

Within the family of interface capturing methods, the Level-Set (LS) method [3] and the Volume-of-Fluid (VOF) method [4] are commonly used. The LS method is a technique that utilizes a continuous LS function, representing the shortest signed distance from an interface, to capture and track interfaces in two-phase flow simulations. This method provides accurate calculation of the unit normal vector, curvature, and surface tension of the interface due to precise spatial gradient calculations. However, this method is known to have issues with mass conservation, which may lead to inadequate capturing of dynamic interfaces in the presence of phase change. Such limitations can challenge accurate predictions of local fluid structure and macro-scale flow regime. In contrast, the VOF method employs an indicator function with values ranging between zero and unity to capture the interface and tracks it by solving the continuity equation for the volume fraction of one of the phases. While this approach avoids mass conservation violations, it results in a diffusive interface due to the discontinuous nature of the VOF function across the interface. To overcome the limitations of both LS and VOF methods, their respective merits are combined.

The Coupled Level-Set and Volume-of-Fluid (CLSVOF) method, a hybrid of the LS and VOF methods, was initially introduced by Bourlioux

[5]. Following the validation of its efficacy in modeling two-phase flows with dynamic interfacial phenomena, including merging, pinching, and droplet falling by Sussman and Puckett [6], this method has emerged as a promising approach for simulating two-phase flows. CLSVOF benefits from the improved mass conservation attribute of VOF while also adopting a continuous and smooth LS function that accurately calculates surface tension force, thereby facilitating the precise capture and simulation of small bubble dynamics, fluid motion, and heat transfer. In contrast, for VOF, the calculation of interface normal vector and curvature relies on the spatial derivative of the volume fraction, which compromises the representation of the interface. The effectiveness of the CLSVOF method were further underscored in the study by Gerlach et al. [7]. The research revealed that CLSVOF effectively mitigates parasitic currents, offering a cost-efficient computational approach with a user-friendly implementation process. In essence, CLSVOF showcased its potential as a dependable interface tracking method, particularly suited for extensive-scale applications, paralleling the context of the present study.

A review of the pertinent literatures regarding the use of the CLSVOF method for simulating heat and mass transfer in boiling situations is presented herein. Ningegowda and Premachandran [8] performed validation of the CLSVOF method with improved advection algorithms for non-uniform grids to reduce computational costs. Their multi-directional advection method carries out interface reconstruction and re-initialization processes at once for all directions, which was reported to reduce computational cost by twice and thrice for 2-D and 3-D, respectively, when compared to conventional operator-splitting methods. They applied this method to simulate various two-phase flow phenomena such as static bubbles, periodic bubble release from a vapor film, rising bubble in bulk liquid, and Rayleigh–Taylor instability. Of those, the performance of the CLSVOF-CSF model was evaluated against saturated film flow boiling data, where the model prediction showed 8.993–13.412% over-prediction when compared to empirical correlations, highlighting the efficacy of the model. The CLSVOF method has been successfully extended to model multiple bubbles during saturated film boiling. Balcázar et al [9] utilized the CLSVOF method and assessed its ability to simulate incompressible two-phase flows on unstructured meshes. From the comparison of their simulation result against experimental images, CLSVOF was validated to be robust enough to perform high accuracy computations for interfacial flows. Furthermore, enhanced mass conservation property of CLSVOF is also validated with an error less than 10^{-5}. Pandey et al. [10] demonstrated the capability of the CLSVOF model to capture the interface morphology of multiple rising bubbles under different gravity levels, ranging from 0.16 to 1.0 of Earth gravity. Their numerical simulations predicted larger size and height of the rising bubble and deteriorating heat transfer rate with decreasing gravity. Even though they showed the potential of the CLSVOF model by demonstrating the model's ability to capture interfacial morphology of multiple bubbles, due to the absence of validation via flow visualization, the performance of the CLSVOF model still required further investigation. The superior interfacial tracking performance of the CLSVOF model was prominently showcased in research conducted by Lorenzini and Joshi [11,12]. They performed a direct comparison between the conventional VOF model and the advanced CLSVOF model in the context of simulating flow boiling within a micro-heat exchanger. Their study revealed that the CLSVOF model outperformed the standard VOF model in accurately predicting the complex interfacial behavior of the vapor phase within the heated zone. The CLSVOF model demonstrated the ability to predict smoother bubble profiles, which were found to be in excellent agreement with experimental flow visualizations. This comparative investigation highlights the improved accuracy and capability of the CLSVOF model in capturing intricate vapor-phase dynamics in flow boiling scenarios. The CLSVOF method has also been used to investigate the condensation of multiple bubbles in subcooled liquid bath, demonstrating its ability to predict complex dynamic behavior of multiple bubbles under varying liquid-phase velocity and temperature fields [13]. Most recently, Kim et al. constructed a CFD model utilizing the CLSVOF method coupled with *bubble collision dispersion* (BCD) *force* for simulating cryogenic flow boiling using liquid nitrogen [14]. The utilization of the CLSVOF model with the BCD force was found to overcome several limitations of previous VOF-based models and yield excellent predictions of wall temperatures along a heated tube. The maximum deviation of the predicted wall temperatures from the measured values was reported to be only 1.67 K, showcasing the high accuracy achieved by the model. Moreover, the CLSVOF model, in conjunction with the BCD force, demonstrated exceptional capability in accurately predicting void fraction development, further validating its effectiveness in capturing the complex interfacial behavior and flow characteristics in flow boiling applications.

Bubble nucleation occurs during the boiling process when cavities on the heated surface reach a required wall superheat to initiate nucleation. The growth of the bubble begins after nucleation and eventually the bubble detaches from the heated wall. Heterogeneous nucleation is commonly observed, as bubbles are formed at different evaporation rates due to variations in local temperature and pressure caused by surface roughness or impurities. The time required for the formation of a new bubble at the nucleation site is also significant, as it can have a direct impact on the heat removal process by latent heat. Hsu and Graham [15] introduced the concept of waiting time for bubbles to form on a heated surface during boiling. The departure of bubbles ruptures the thermal boundary layer, and new bubbles are nucleated after the liquid in the vicinity of the heated surface achieves the required superheat and the cycle is repeated. The mechanisms of bubble nucleation and bubble departure are quite complex and can be influenced by several factors, such as surface roughness, nucleation site density, and local fluid temperature and pressure conditions.

Unfortunately, incorporating the bubble nucleation cycle into the numerical simulation presents a formidable challenge. Attempts have been made to simulate the bubble nucleation in conjunction with previously introduced interface capturing methods. One approach to computationally simulate bubble nucleation behavior is to artificially create cavities or micro-structures on the heated surface. Jafari and Okutucu-Özyurt [16] investigated subcooled flow boiling by creating a single artificial cavity on the heated surface to examine its effects on boiling initiation, bubble growth, and departure. However, the suggested method is limited in that it does not fully replicate real-life flow boiling scenarios where multiple cavities of different shapes and sizes are present along the heated surface. Lin et al. [17] numerically investigated the effect of micro-fins and micro-cavities on subcooled flow boiling in perspective of pressure drop, heat transfer coefficient, and thermal resistance. They reported that, by employing the micro-fin structures, 12.74% higher pressure drop, 61.92% higher heat transfer coefficient, and 36.64% lower thermal resistance were achieved. Moreover, by utilizing the micro-cavity structures, 4.36% higher pressure drop, 17.16% higher heat transfer coefficient, and 13.55% lower thermal resistance were achieved, revealing the overall impact of varying wettability of the heated surface.

While generating artificial cavities could be useful in studying bubble nucleation process, it is limited to scenarios where the number, size, and location of cavities are known, such as rise of a single bubble. Chen et al. [18] employed an alternative approach of generating an artificial bubble nucleus on the heated surface to study subcooled water flow boiling. The nucleation sites were pre-determined on the mesh nodes and activated by the degree of wall superheat. They successfully predicted the evolution of the flow regime from bubbly to slug along the heated length. While this is valid for the flow boiling of water, the same models are inapplicable to other fluids, such as nPFH, since they utilize a nucleation density correlation specifically developed for water. Similarly, by applying the Eulerian-Eulerian two-fluid model, Cheung et al. [19] assessed the heat partitioning model along with various empirical correlations for closure relations to simulate subcooled water flow boiling. The best performing empirical correlations were suggested for

each physical parameter, including active nucleation site density, bubble departure diameter, and bubble departure frequency correlations. However, as listed in Table 2, suggested empirical correlations in both studies are focused only on water, all of which are difficult to adapt for other fluids, such as the highly wetting nPFH. Incorporating similar effects in dielectric fluid simulations would require conducting future experiments with careful measurements of bubble departure diameter, bubble nucleation site density, and bubble departure frequency for each combination of dielectric fluid and solid wall material. These experimental data would be essential to develop accurate models and simulations for dielectric two-phase flow boiling systems. Limitations for applying the empirical bubble nucleation models in flow boiling simulations have been comprehensively summarized by Kim et al. [14]. In addition to macroscopic large-scale studies of flow boiling, such as the present study, alternative research endeavors have been pursued by Chen et al. [20,21] to gain a microscopic understanding of bubble nucleation. In their investigations, they conducted an in-depth examination of the impact of surface wettability on bubble nucleation time and growth rate. They employed theoretical calculations and molecular dynamic simulations, providing valuable insights into the intricate processes of bubble nucleation on grooved substrates with varying wettability.

Over the years, PU-BTPFL investigators have conducted a series of comprehensive investigations of hydraulic and heat transfer characteristics of flow boiling utilizing Computational Fluid Dynamics (CFD). Initially, using VOF, 2-D computation were performed to assess the capabilities of CFD [22]. The impact of grid size near the wall on bubble nucleation and the ability of the multiphase method to predict boiling flow in combination with an interfacial phase change model were discussed. However, due to inherent limitations in 2-D computations, subsequent work was expanded to 3-D domain, also using VOF, to explore the effects of an additional source term in the momentum equation, shear-lift force, for improved prediction of near-wall bubble dynamics [23]. To verify the efficacy of the added source term, the study simulated a single bubble's lift-off and trajectory after detachment. From a careful examination and comparison of the results with experimental data, the CFD model, coupled with the shear lift force, showed the most accurate prediction of the bubble trajectory compared to simple VOF without the shear lift force. This clearly demonstrated the necessity of incorporating shear lift force in assisting the under-represented bubble lift-off in VOF model, which ultimately aided in preventing premature prediction of CHF by providing more realistic bubble departure behavior and accurate heat transfer. The improved bubble behavior then prompted investigations into key heat transfer mechanisms, hydrodynamic characteristics of critical heat flux (CHF), and flow boiling in microgravity, leading to enhanced predictions of two-phase flow pattern and heat transfer [24,25]. More recently, another important yet under-represented additional momentum source term, namely bubble collision dispersion force, was incorporated into flow boiling CFD models. Lee et al. [26] and Kim et al. [14] developed a new user defined function (UDF) and adapted the bubble collision dispersion force to improve the accuracy of predicting the bubble distribution along and across the flow channel during flow boiling simulations. Notably, in the case of horizontal flow boiling of nPFH, the inclusion of the bubble collision dispersion force resulted in accurate prediction of the flow structure by suppressing excessive bubble merging and diminishing vapor accumulation near the top surface. Furthermore, Kim et al. [14] provided a quantitative demonstration of the effect of the bubble collision dispersion force by comparing the predicted outlet void fraction with and without the force, which verified the inclusion of the bubble collision force to offer far more accurate flow structure and axial void fraction profiles for flow boiling simulations. These successive research efforts have contributed to a deeper understanding of flow boiling phenomena and the development of more accurate predictive models using CFD.

1.3. Objectives of study

This study provides a detailed analysis of CFD simulations of flow boiling along a rectangular channel using n-perfluorohexane (nPFH, C_6F_{14}) as working fluid under microgravity conditions. Unlike the authors' prior work, the present investigation is primarily focused on operating conditions involving low inlet subcooling and a double-sided heating configuration. To establish the reliability of the CFD model, the obtained results are rigorously validated against experimental data encompassing both heat transfer measurements and high-speed video recordings of interfacial behavior. Subsequently, the validated CFD models are employed to predict the fluid flow and heat transfer characteristics for the specified operating conditions, all of which are for microgravity environment. Thereby, the numerical study provides valuable insights into the underlying physical processes governing the flow boiling phenomenon of nPFH in a reduced gravity environment.

A key innovation with the computing method adopted in the present study is the ability to circumvent the fundamental weakness of VOF by accounting for important effects of shear lift force, bubble collision dispersion force, and drag force, in addition to utilizing the advanced interfacial tracking of CLSVOF. The combination of CLSVOF and additional momentum source terms has not been attempted before for microgravity flow boiling simulations.

Key objectives of this study are to:

(1) Implement CLSVOF for microgravity flow boiling simulations to better capture two-phase interfacial structure and behavior.
(2) Incorporate shear lift force, bubble collision dispersion force, and drag force UDFs into microgravity flow boiling simulations to assist under-represented bubble dynamics in single momentum equation models.
(3) Validate predictions of the new model against microgravity data from the Flow Boiling Experiment (FBCE) conducted on the International Space Station (ISS).
(4) Utilize high resolution CFD predictions to investigate spatial variations of interfacial flow pattern, fluid temperature, and fluid velocity, flow characteristics that are very difficult to measure from experiments.

2. Experiment methods

2.1. FBCE and flow boiling module (FBM)

This study constitutes a collaborative endeavor involving PU-BTPFL and NASA Glenn Research Center, which commenced in 2011 with the primary objective of developing the Flow Boiling and Condensation Experiment (FBCE). FBCE stands as NASA's largest and most intricate phase change facility devised hitherto for conducting experiments under microgravity; FBCE was successfully deployed on the International Space Station (ISS) in 2021. The fundamental purpose behind this deployment is to gain comprehensive insights into the ramifications of microgravity on flow boiling and flow condensation phenomena. To facilitate validation of the CFD model employed in this investigation, data acquired from experiments conducted aboard the ISS are utilized. The experimental setup and procedures of the FBCE have been meticulously documented in Mudawar et al. [27]. However, for the sake of clarity and ease of comprehension, a concise summary of the experimental configuration is provided herein, serving to enhance the comprehension of the results obtained in this study.

The primary apparatus responsible for data acquisition in this facility is the Flow Boiling Module (FBM), which is depicted in Fig. 1(a). The FBM is specifically designed to measure the pertinent fluid flow and heat transfer characteristics while concurrently recording interfacial behavior via high-speed video at a frequency of 2000 frames per second. The overall configuration of the experimental facility comprises multiple subassemblies, as illustrated in Fig. 1(b). These were transported to

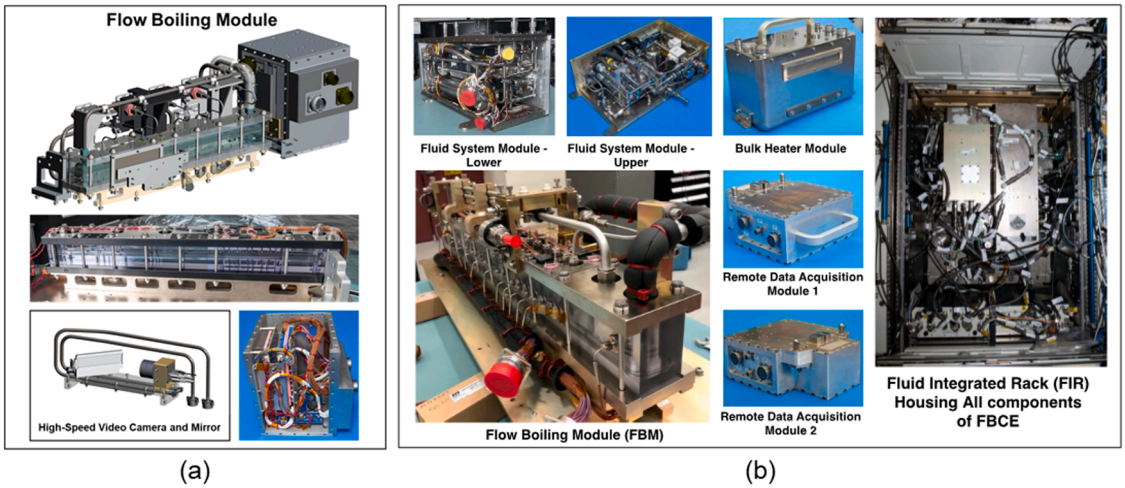

Fig. 1. (a) Image and CAD renderings of the Flow Boiling Module (FBM), and (b) Images of FBCE's subassemblies and Fluid Integrated Rack (FIR).

the International Space Station (ISS) utilizing Northrop Grumman's Antares Rocket and subsequently integrated within the Fluid Integrated Rack (FIR) situated onboard the ISS.

In Fig. 2(a), an elaborate depiction of the Flow Boiling Module (FBM) design is presented. The FBM is comprised of three polycarbonate plastic (Lexan) plates that are tightly compressed between two aluminum support plates, with two oxygen-free copper slabs inserted into specifically milled slots within the upper and lower polycarbonate plates. To ensure leak-free operations, O-ring seals are meticulously placed within grooves in the Lexan plates. Upstream, a honeycomb flow straightener is affixed to facilitate streamlining of the incoming flow and to eliminate undesirable eddies. To achieve controlled heating, a series of resistive heaters is soldered to the rear surface of each copper slab, thereby effectively heating the fluid along the designated heated length of L_h = 114.6 mm. The flow channel present within the middle polycarbonate plate is of rectangular cross-section with dimensions of W = 2.5 mm and H = 5.0 mm, permitting heating along either one or both of its shorter walls. To ensure fully developed flow upstream of the heated section, an upstream entry length of L_d = 327.9 mm is used, and a downstream adiabatic length of L_e = 60.7 mm follows the heated length. Fig. 2(b) presents a comprehensive view of the constructed copper slabs, highlighting the arrangement of six resistive heaters attached to the rear surface of each slab to ensure uniform axial heating. The 188-Ω resistive heaters on each copper slab are electrically connected in parallel and are supplied power by a variable voltage transformer. Fig. 2(c) demonstrates the installation of two sets of seven type-E thermocouples, placed within shallow holes along the centerline of each copper slab just upstream and downstream of each resistor. The longer sidewalls *(H)*, constructed of insulating polycarbonate plastic, are adiabatic and transparent, serving as viewports for high-speed video imaging of interfacial characteristics along the flow channel's heated length. For more detailed information on the experimental setup, operational procedures, flow visualization techniques, instrumentation details, and measurement uncertainty, readers are encouraged to refer to Mudawar et al. [27].

It is essential to emphasize that all experimental data employed in this study employed a double-sided heating configuration where heating was consistently applied along both opposite short walls (*W*). The author's previous horizontal flow boiling study [26], with an emphasis on stratification effects in Earth gravity, adopted the single-sided heating configuration. This deliberate choice stems from the need to isolate the distinct influences of body forces acting perpendicular and parallel to the heated wall on heat transfer and flow physics. Conversely, the use of double-sided heating, involving the simultaneous heating of two opposite walls, introduces greater complexity to the flow boiling phenomenon. The presence of vapor bubbles generated along both walls leads to mutual interactions between these bubbles, significantly altering the flow physics throughout the channel. This complexity arises due to the interplay of two distinct heating sources, resulting in complex flow patterns and heat transfer dynamics that require thorough investigation and analysis. Therefore, this study places a dedicated emphasis on analyzing and comprehending the intricate interfacial interactions induced by the two opposite heated walls. Note that heating more than two of the four walls would adversely affect the quality of flow visualization of the interfacial features, which plays crucial role in validating the CFD model employed in this study.

2.2. Data processing

Steady-state data points are obtained by taking the average of the steady portions of the temporal data recorded by the data acquisition system. Thereafter, additional post-processing is performed using fluid properties obtained from NIST-REFPROP [28].

At the inlet of the FBM, the fluid exists in a subcooled liquid state, and the corresponding fluid enthalpy is directly ascertained from the FBM inlet fluid temperature, T_{in}, and pressure, p_{in}, as

$$h_{in} = h|_{T_{in},p_{in}} \tag{1}$$

At the outlet of the FBM, the fluid may contain some vapor, and its enthalpy is computed using

$$h_{out} = h_{in} + \frac{q'' P_h L_h}{\dot{m}} \tag{2}$$

which involves performing an energy balance over the FBM. Here, q'' represents the wall heat flux from wetted surface of the copper slabs, $\dot{m}$ mass flow rate, and P_h heated perimeter (2 W).

The thermodynamic equilibrium qualities at both the FBM inlet and outlet are determined as

$$x_e = \frac{h - h_f|_p}{h_{fg}|_p} \tag{3}$$

where $h = h_{in}$ or h_{out} is the actual fluid enthalpy at the FBM inlet/outlet, and both h_f, the saturated liquid enthalpy, and h_{fg}, the latent heat of vaporization, are evaluated at the measured inlet/outlet pressure.

Local wall temperatures, designated as $T_{wi,z}$, where w_i is the heated wall (w_1 or w_2) and z is the streamwise measurement location (1 upstream through 7 downstream) are shown in Fig. 2(c). Each local wall temperature, T_w, is calculated from the corresponding measured thermocouple temperature, T_{tc}, by assuming a uniform heat flux and one-

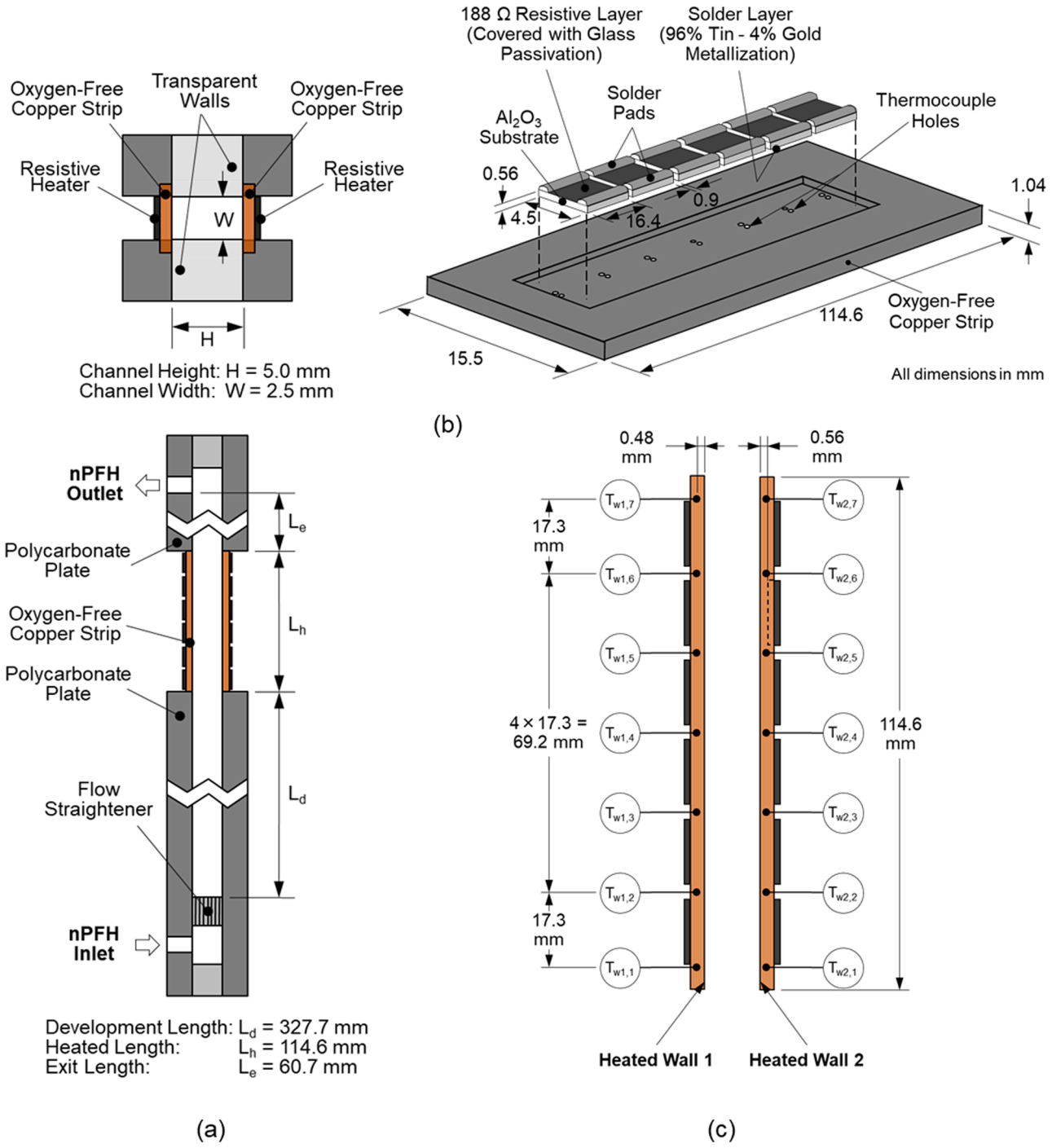

Fig. 2. Schematic representations of (a) overall construction of Flow Boiling Module (FBM), (b) construction of heating strips, and (c) designation of heated walls and local wall temperatures.

dimensional heat conduction through distance H_{tc} (=0.48 mm) within pure copper of thermal conductivity, k_s, as

$$T_w = T_{tc} - \frac{q'' H_{tc}}{k_s} \tag{4}$$

Both saturation temperature, $T_{sat,z}$, and thermodynamic equilibrium quality, $x_{e,z}$, at these locations are determined using linear interpolation between values at the inlet and outlet. The heated single-phase length is estimated using

$$L_{h,sp} = \frac{GA_c}{q'' P_h}\left(h_{f,P_{in}} - h_{in}\right) \tag{5}$$

where A_c is the channel's cross-sectional area, and saturation temperature at the end of $L_{h,sp}$ (i.e., at location where $x_e = 0$) is estimated by linear interpolation as

$$T_{sat,x=0} = T_{sat}|_{p_{in}} + \left(T_{sat}|_{p_{out}} - T_{sat}|_{p_{in}}\right)\frac{L_{h,sp}}{L_h} \tag{6}$$

The fluid temperature at the streamwise locations is estimated based on the local fluid state as

$$T_{f,z} = \begin{cases} T_{in} + \left(T_{sat,x=0} - T_{in}\right)\dfrac{z}{L_{h,sp}}, & x_{e,z} < 0 \\ T_{sat,z}, & 0 \le x_{e,z} \le 1 \end{cases} \tag{7}$$

3. Computational methods

3.1. Computational sub-models and governing equations

This study employs transient analysis in ANSYS-Fluent to investigate flow boiling in a rectangular channel heated along two opposite walls, under zero gravity and low inlet subcooling conditions. The dynamic behavior of two-phase fluid flow and heat transfer both across and along the heated length of the flow channel is tracked through the transient analysis. To capture detailed interfacial structure, interface tracking is incorporated by means of the *Lee mass transfer* model [29] and *Continuous Surface Force* (CSF) model [30] with the transient CLSVOF method. Additionally, the *Geo-Reconstruction scheme*, also known as the piecewise-linear method, and *anti-diffusion treatment* [31] are employed, respectively, to achieve sharp interface morphology and prevent false interfacial distortion induced by numerical diffusion. The *Shear-Stress Transport* (SST) $k-\omega$ turbulence model, which also accounts for viscous heating, is used to address turbulence and eddy dissipation effects.

Despite the widespread use of VOF for two-phase simulations, interfacial forces governed by relative motion between phases are not accurately accounted for because of using a single momentum equation for both liquid and vapor phases. To improve the predictive capability of single momentum equation CFD models, it is crucial to incorporate additional momentum source terms that are not captured by the shared velocity and pressure fields. To compensate for the inherent limitations of the VOF method, the present simulations include additional important force terms, namely (i) *shear-lift*, (ii) *bubble collision dispersion*, and (iii) *drag*. Further details on governing equations and physics of the models are discussed in the following sections.

3.1.1. Governing equations

Mass conservation for each phase is expressed in terms of the temporal variation and advection of the corresponding volume fraction, balanced by net mass transfer into and out of each cell,

$$\frac{\partial \alpha_f}{\partial t} + \nabla\cdot\left(\alpha_f \vec{u}_f\right) = \frac{1}{\rho_f}\sum\left(\dot{m}_{gf} - \dot{m}_{fg}\right) \tag{8}$$

and

$$\frac{\partial \alpha_g}{\partial t} + \nabla\cdot\left(\alpha_g \vec{u}_g\right) = \frac{1}{\rho_g}\sum\left(\dot{m}_{fg} - \dot{m}_{gf}\right) \tag{9}$$

where α, t, u, ρ, and $\dot{m}$, are volume fraction, time, velocity, density, and mass transfer rate by evaporation (with subscript of *fg*) and condensation (with subscript of *gf*), respectively. Notice that the sum of void fractions for the individual phases in each cell is equal to unity, meaning the Eq. (9) is not solved and the liquid volume fraction is computed as $\alpha_f = 1 - \alpha_g$. The physical properties appearing in the governing equations are expressed as functions of properties of individual phases weighted with respect to the volume fraction. Excess numerical diffusion in interfacial cells, which can arise from fluid advection in high-aspect-ratio cells, is suppressed by *anti-diffusion treatment,* adding a negative diffusion source term, $-\nabla\cdot(\vec{u}_c\alpha(1-\alpha))$, in the volume fraction equation, where $\vec{u}_c$ is compressive velocity that prevents dispersion in the direction normal to the interface.

A hallmark characteristic of the CLSVOF method is its incorporation of surface tension force in the momentum equation, which sets it apart from the VOF method. But, like the VOF treatment, the CLSVOF method entails solving a single momentum equation for the mixture using pseudo-mixture properties, which is expressed as

$$\frac{\partial}{\partial t}(\rho\vec{u}) + \nabla\cdot(\rho\vec{u}\vec{u}) = -\nabla P + \nabla\cdot\left[\mu\left(\nabla\vec{u} + \nabla\vec{u}^T\right)\right] - \sigma\kappa\delta(\varphi)\nabla\varphi + \vec{S}_M \tag{10}$$

where σ, κ, φ, P, μ, and S_M are surface tension, interface curvature, level set function, pressure, dynamic viscosity, and momentum source term, respectively. Since this study considers zero gravity conditions, the term related to the gravitational force is eliminated.

Similarly, energy conservation in the CLSOVF method is identical to that in the VOF method, and is expressed as

$$\frac{\partial}{\partial t}(\rho E) + \nabla\cdot(\vec{u}(\rho E + P)) = \nabla\cdot\left(k_{eff}\nabla T\right) + S_E \tag{11}$$

where E, k_{eff}, T, and S_E refer, respectively, to internal energy, temperature, effective conductivity, and heat source term, the latter being the mass transfer rate multiplied by the latent heat of vaporization.

The Lee model [29] has demonstrated exceptional versatility in tackling various phase change configurations and broad ranges of operating conditions through a comparatively straightforward formulation for mass transfer rate by evaporation and condensation, expressed as respectively, by the relations

$$\dot{m}_{fg} = r_e\alpha_f\rho_f\frac{\left(T_f - T_{sat}\right)}{T_{sat}} \text{ for evaporation} \tag{12}$$

and

$$\dot{m}_{gf} = r_c\alpha_g\rho_g\frac{\left(T_{sat} - T_g\right)}{T_{sat}} \text{ for condensation,} \tag{13}$$

where r_e and r_c are the *mass transfer intensity factors* for evaporation and condensation, respectively, whose magnitude plays a crucial role in the model. A major challenge in calculating interfacial mass transfer rate arises due to the dependence on the magnitudes of mass transfer intensity factors, which are neither theoretically determined nor universal. Therefore, the values of r_e and r_c must be judiciously selected based on flow configuration and geometry, working fluid, and operating conditions, while ensuring a minimal temperature difference between the interface and saturated vapor and preventing numerical divergence. Ultimately, optimum values for r_e and r_c are determined through a careful comparison of CFD predictions with *both* measured wall temperature and video-captured interfacial behavior along the channel. The impact of the magnitude of mass transfer intensity factors was extensively discussed in recent PU-BTPFL works [22,23] for the same flow channel geometry examined in the present study, culminating in the values of $r_e = 100$ and $r_c = 20$ for highly subcooled inlet conditions and operation in Earth gravity. Identical values are adopted in the present study for conditions of low inlet subcooling.

3.1.2. Interface topography representation

The ability of the CLSVOF method to furnish more precise interface topology is crucial to achieving an accurate simulation of surface tension force. This, in turn, improves the precision of predicting the overall force balance on individual bubbles, facilitating more precise forecasting of the bubble formation cycle from nucleation to detachment. As elucidated in Eq. (14) below, the level-set function, φ, utilized in CLSVOF, is defined as a signed distance, d, to interface, and is positive for the primary liquid phase and negative for the secondary vapor phase, with the interface explicitly designated as $\varphi = 0$.

$$\varphi(x,t) = \begin{cases} +|d| & \text{if } x \text{ belongs to primary phase} \\ 0 & \text{if } x \text{ belongs to interface} \\ -|d| & \text{if } x \text{ belongs to secondary phase} \end{cases} \tag{14}$$

This formulation imparts a smooth and continuous character to the level-set function across the interface. In the CLSVOF method, the interface normal vector, $\vec{n}$, and curvature, κ, are computed based on the

formulation below,

$$\vec{n} = \left.\frac{\nabla\varphi}{|\nabla\varphi|}\right|_{\varphi=0} \tag{15}$$

and

$$\kappa = \nabla\cdot\left.\frac{\nabla\varphi}{|\nabla\varphi|}\right|_{\varphi=0} \tag{16}$$

which represents a fundamental advantage over the VOF method, where the calculation of interface normal vector and curvature is based on the spatial derivative of volume fraction, which is intrinsically discontinuous across the interface, leading to an imprecise representation of the interface [32]. With reliance on the smooth and continuous level set function across the interface, the CLSVOF method enables the precise calculation of surface tension force, thereby facilitating a more accurate depiction and simulation of small bubble dynamics, fluid motion, and heat transfer. In the present simulations, the computation of surface tension is grounded on the *Continuum Surface Force* (CSF) model.

3.1.3. Additional momentum equation terms

3.1.3.1. Surface tension. Surface tension effects at interfaces are modeled by incorporating an addition force term S_{st} which is calculated using the *Continuum Surface Force (CSF)* model [30],

$$S_{st} = \sigma\frac{\rho_m\kappa\delta(\varphi)}{0.5\left(\rho_f+\rho_g\right)} \tag{17}$$

where ρ_m and σ are the volume-averaged density of the mixture and the surface tension, respectively, and κ is the interface curvature. The function of $\delta(\varphi)$ is given by

$$\delta(\varphi) = \begin{cases} \dfrac{1+\cos\left(\dfrac{\pi\varphi}{a}\right)}{2a} & \text{if } |\varphi| \le 0 \\ 0 & \text{if } |\varphi| \ge 0 \end{cases} \tag{18}$$

wherein $a = 1.5$ h, h being the grid spacing. The magnitude of contact angle is determined by the wall superheat, ΔT_w, according to [33]

$$\theta_w = 17.4(\Delta T_w)^{0.323} \tag{19}$$

3.1.3.2. Shear-lift force. To improve the prediction of near-wall bubble behavior and thus heat transfer, the shear-lift force formulation by Mei and Klausner [34] is employed as a source term in the momentum equation using a user-defined function (UDF) in ANSYS-Fluent. A correlation was developed using data for a wide range of Reynolds numbers and is given as

$$S_{sl} = \frac{1}{8}\pi C_L\rho_f u_r^2 d_b^2 \tag{20}$$

where

$$C_L = 3.877G_s^{1/2}\times\left[\mathrm{Re}_b^{-m/2} + \left(0.344G_s^{1/2}\right)^m\right]^{1/m},\ \text{with}\ m = 4, \tag{21}$$

and

$$G_s = \frac{1}{2}\left|\frac{du_r}{dy}\right|\frac{d_b}{u_r}, \tag{22}$$

In the equations above, G_s is the dimensionless shear rate based on relative velocity u_r $(=u_f - u_g)$ between the vapor bubble and liquid, d_b is the bubble diameter, and Re_b is the bubble Reynolds number based on bubble diameter as characteristic length.

3.1.3.3. Bubble collision dispersion force. Sharma et al. [35] modeled the turbulence-induced *bubble collision force* responsible for bubble diffusion without significant coalescence. This force was shown to describe the lateral movement of bubbles in flow boiling and resulted in a flatter void fraction profile in the channel's cross-section. Note that bubbles can be classified into two major groups [36]: (i) spherical and distorted bubbles, and (ii) slug and churn-turbulent bubbles. The original formulation of the bubble collision dispersion force model is best suited for bubbly flow, which is dominant in the present study. According to [35], the bubble collision dispersion force per unit volume of mixture can be modeled and computed according to

$$S_c = -\left(K\frac{\rho_f u_t^2}{2\alpha_{\max}^{2/3}}\right)f(\alpha)\nabla\alpha \tag{23}$$

where $\alpha_{\max}$ and K are the *dense packing limit* and a proportionality constant, with recommended values for bubbly flow of 0.62 and 1, respectively. Also in Eq. (21), u_t is liquid fluctuating velocity due to liquid agitation, which represents effects of turbulence intensity on bubble dispersion, and $f(\alpha)$ is defined as

$$f(\alpha) = \alpha^{2/3}\left[1-\left(\frac{\alpha}{\alpha_{\max}}\right)^{1/3}\right]^{-1} \tag{24}$$

The liquid fluctuating velocity, u_t, in Eq. (23) is determined by net velocity difference between vapor phase velocity at each cell and average velocity of liquid flow, which is updated every iteration. More details and the effect of the force on flow boiling are described in a prior PU-BTPFL study [14].

3.1.3.4. Drag force. A drag force is applied to vapor bubbles whose velocity is lower than liquid velocity, and it is given by

$$S_D = \frac{3}{4}C_D\frac{\rho_f\alpha u_r|u_r|}{d_b} \tag{25}$$

where C_D is the drag coefficient. According to Ishii and Zuber [37], the drag coefficient in Eq. (25) is generally dictated by prevailing bubble shape regime, which is classified in gas-liquid flows into three categories: viscous, distorted particle, and cap bubble, the latter two being highly influenced by gravity. However, due to the operating conditions of zero gravity, the relation for C_D adopted in this study is the one recommended for the viscous regime, and is given by

$$C_D = \frac{24}{\mathrm{Re}_b}\left(1+0.15\mathrm{Re}_b^{0.75}\right) \tag{26}$$

where,

$$\mathrm{Re}_b = \frac{\rho_f|u_r|d_b}{\mu_f} \tag{27}$$

3.1.3.5. User-defined function (UDF) adaptation. All the details for calculating and implementing the momentum terms in UDF are provided in a prior PU-BTPFL study [38]. With the fluid entering the heated section of the flow channel in a subcooled liquid state, the shear lift is encountered even in the upstream region. After initiation of the phase change, the algorithm discerns cells characterized by a vapor phase volume fraction and computes the aggregate vapor volume throughout the entire domain via summation of vapor cells. Concurrently, it ascertains the cumulative face areas wherein vapor interfaces with the thermally conjugated surface demarcate fluid and solid cells. These values are sequestered in allocated memory, accessed by the UDF, and subsequently utilized to deduce the mean vapor diameter during each numerical iteration by dividing the aggregate vapor cell volume by the cumulative vapor surface area. In light of the fluid's entry into the heated portion of the channel in a subcooled liquid state, the bubble collision dispersion force remains inexistent in the inlet region initially. Upon the inception of phase change, the UDF algorithm identifies cells

exclusively occupied by liquid (exhibiting zero void fraction) and iteratively processes the identified liquid cells to compute a volume-averaged mean liquid velocity. Employing the local velocity for each vapor cell, the liquid fluctuating velocity—alternatively termed *agitation velocity*—is ascertained as the absolute difference between the mean liquid velocity and local vapor velocity. The agitation velocity is saved in allocated memory and subsequently recalled during the computation of the bubble collision dispersion force, which is exclusively applied at the liquid-vapor interface. To accomplish this, the algorithm discerns the liquid-vapor interface by pinpointing cells with a void fraction ranging from 0 to 1. For the identified cells, the agitation velocity and gradient of vapor volume fraction, $\nabla\alpha$, are harnessed to compute the force. This force is subsequently integrated as a source term within the momentum conservation equation.

3.2. Computational domain and boundary conditions

The 3-D CFD model utilized in this study precisely incorporates the geometric design of the rectangular flow channel, featuring a cross-section of 5.0 mm × 2.5 mm and a length of 129.6 mm, accounting for the actual positioning of the six discrete heaters on each copper slab, as depicted in Fig. 3(a). The computational domain encompasses an upstream adiabatic entry length of $L_{entrance} = 5$ mm, a heated length $L_h =$ 114.6 mm, and an adiabatic exit length of $L_{exit} = 10$ mm. The copper slab's width and thickness are 15.5 mm and 1.04 mm, respectively.

Given that the predictive accuracy of fluid flow and heat transfer characteristics is significantly influenced by mesh size, a meticulous series of grid size iterations is conducted until a size is reached that ensures solution convergence. The employed mesh consists of 938,592

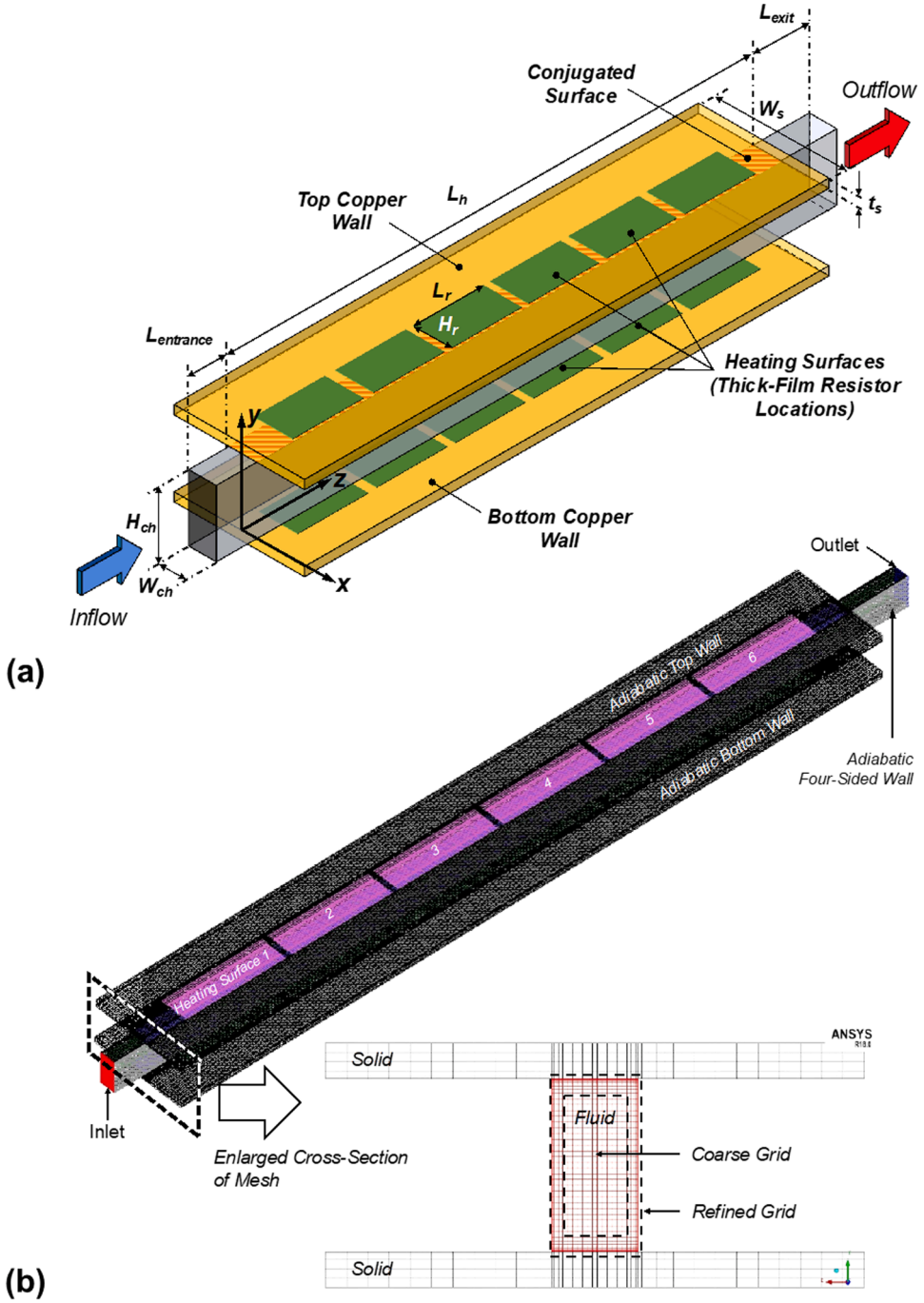

Fig. 3. (a) Schematic of 3D computational geometry. (b) Mesh configuration in full domain and cross-section area [38].

Table 1
Operating conditions employed in the CFD simulations for n-PFH flow boiling.

Test case	G (kg/m^2 s)	P_{in} (kPa)	q'' (W/m^2)	CHF (W/m^2)	$T_{sat,in}$ (°C)	$\Delta T_{sub,in}$ (°C)	$x_{e,in}$
1	199.9	132.8	48,489	182,342	65.4	4.9	−0.07
2		139.1	118,686	182,342	66.8	6.2	−0.08
3	799.9	131.2	68,006	314,340	65.0	3.8	−0.05
4		141.5	202,512	314,340	67.4	5.8	−0.08
5	2399.9	128.3	113,256	392,479	64.3	4.0	−0.05
6		137.4	231,056	392,479	66.4	5.7	−0.08

quadrilateral cells and 1,030,800 nodes. As depicted in Fig. 3(b), the near-wall region mesh is refined to a grid size of $\Delta c = 0.006$ mm to accurately capture critical fluid flow and heat transfer features, including shear stress, thermal diffusion, and vapor growth, while a coarser yet uniform mesh with $\Delta c = 0.166$ mm is adopted for the core region. Grid independence and $y+$ values for this domain have been verified in the authors' previous studies [23,25]. Additionally, grid convergence analysis results through successive refinements are described in [22], which indicated a near-wall cell size below 14 μm yields grid-independent outcomes. Consequently, four distinct grids along the flow channel's height are examined in 3-D to determine the optimal mesh for capturing bubble nucleation and accounting for near-wall latent heat transfer. The results reveal that asymptotic convergence of averaged wall temperature is attained using a near-wall cell size below 7.6 μm. Therefore, a cell size of 6.5 μm is adopted in the present study to ensure desired accuracy with minimal computing time. Based on the larger theoretical bubble size of nPFH than that of water, a cell size of 6.5 μm of the current grid system is considered to be effective in capturing the majority of small sized bubbles that are within the focus of this study. Note that recent water flow boiling simulation by Chen et al. [18] utilized 50 μm as initial bubble diameter.

Table 1 presents the details of all simulation cases conducted in this study, using the dielectric fluid n-PFH, focusing on six different combinations of mass velocity and heat flux under ideal zero gravity conditions ($g = 0$). The simulations involve ``double-sided'' heating, wherein both opposite shorter walls (W) of the channel are heated. The tested conditions encompass a range of mass velocities from 199.9 to 2399.9 kg/m^2 s and inlet qualities from −0.05 to −0.08. Constant heat fluxes corresponding to the actual power input from the experiment are applied to six discrete heated regions on each heating wall, aligned with the locations of the thick film resistors. For accurate representation of the heat transfer, a coupled heat flux condition is implemented at the interface between solid and fluid cells to account for conjugate heat transfer appropriately. The other side of the copper wall is designated as an adiabatic boundary. The inlet boundary is defined with fully developed velocity profiles and turbulent intensity calculated based on $I = u'/\overline{u} = 0.16\mathrm{Re}_D^{-1/8}$. The outlet boundary is uniformly set to the experimentally measured outlet pressure. For boundary conditions on solid surfaces, a non-slip condition is applied, and the contact angle (estimated from the vapor-solid interface to the vapor-liquid interface) is determined based on the wall superheat obtained from the experiment. To ensure numerical stability, variable time-step sizes ranging from 10^{-5} to 10^{-7} s are utilized, while maintaining a global Courant number ($u\Delta t/\Delta c$) of unity.

4. Results and discussion

4.1. Partially developed boiling (PDB) and fully developed boiling (FDB)

A recent PU-BTPFL study [38] provided the first assessment of the present CFD method against ISS data, with the entire focus being on *highly subcooled* inlet conditions. The present study continues this assessment by addressing *low inlet subcooling* conditions which, as indicated in Table 1, correspond to $\Delta T_{sub,in} = 3.8$–6.2 °C. The mild subcooling considered here clearly points to earlier bubble nucleation as well as higher void fraction along the channel, meaning overall interfacial behavior and therefore heat transfer characteristics are appreciably different from those for the highly subcooled cases considered in the previous study.

Yet, despite the low inlet subcooling, there will always be an upstream *subcooled boiling region* wherein the liquid gradually acquires sensible heat and the near-wall liquid eventually exceeding local saturation temperature by a finite amount of superheat required to initiate bubble nucleation. This is where the subcooled boiling region is initiated. This region encompasses two sub-regions: upstream *partially developed boiling* (PDB) and downstream *fully developed boiling* (FDB). PDB is defined as a status where nucleating bubbles remain attached to or confined to a close distance from the heated surface due to substantial condensation rendered by the subcooled liquid core. Surpassing the *net-vapor generation* (NVG) location, the boiling regime transitions from PDB to FDB as bubbles commence departure from the surface and void fraction begins increasing at a much larger rate due to an attenuating rate of condensation and an increased number of cavities activated.

Table 2
Representative correlations for bubble nucleation site density, bubble departure diameter, and bubble departure frequency.

	Correlation	Details
Nucleation site density	Li et al. [39] $N_w = N_0(1 - cos\theta)\exp[f(p)]\Delta T_{sup}^{A\Delta T_{sup}+B}$ $f(P) = 26.006 - 3.678\exp(-2P) - 21.907\exp\left(-\frac{P}{24.065}\right)$ $A = -0.0002P^2 + 0.0108P + 0.0119$ $B = 0.122P + 1.988$ $1 - \cos\theta = (1 - \cos\theta_0)\left(\frac{T_c - T_{sat}}{T_c - T_0}\right)$	- Utilized by Chen et al. [18] for subcooled water flow boiling simulation - Developed based on water experiment - Correlates based on wall superheat - - Dimensional pressure correlation
	Mikic and Rohsenow [40] $N_a \sim \frac{C}{D_c^m}$ $D_c = \frac{4\sigma T_{sat}}{\rho_v h_{fg}\Delta T_{sup}}$, $m = 6.5$, $C = D_{c,\max}^m$	- Assessed by Cheung et al. [19] for subcooled water flow boiling simulation - Developed based on water experiment - Correlates based on wall superheat
Bubble departure diameter	Zuber [41] $D_l = \left[\frac{6\sigma}{g(\rho_l - \rho_g)}\frac{kT_{sup}}{Q_w}\right]^{1/3}$	- Assessed by Cheung et al. [19] for subcooled water flow boiling simulation - Developed based on water experiment - Correlates based on wall superheat
Bubble departure frequency	Zuber [41] $f = \frac{1.18}{2D_l}\left[\frac{\sigma g(\rho_l - \rho_g)}{\rho_l^2}\right]^{1/4}$	- Assessed by Cheung et al. [19] for subcooled water flow boiling simulation - Developed based on water experiment - Correlates based on wall superheat

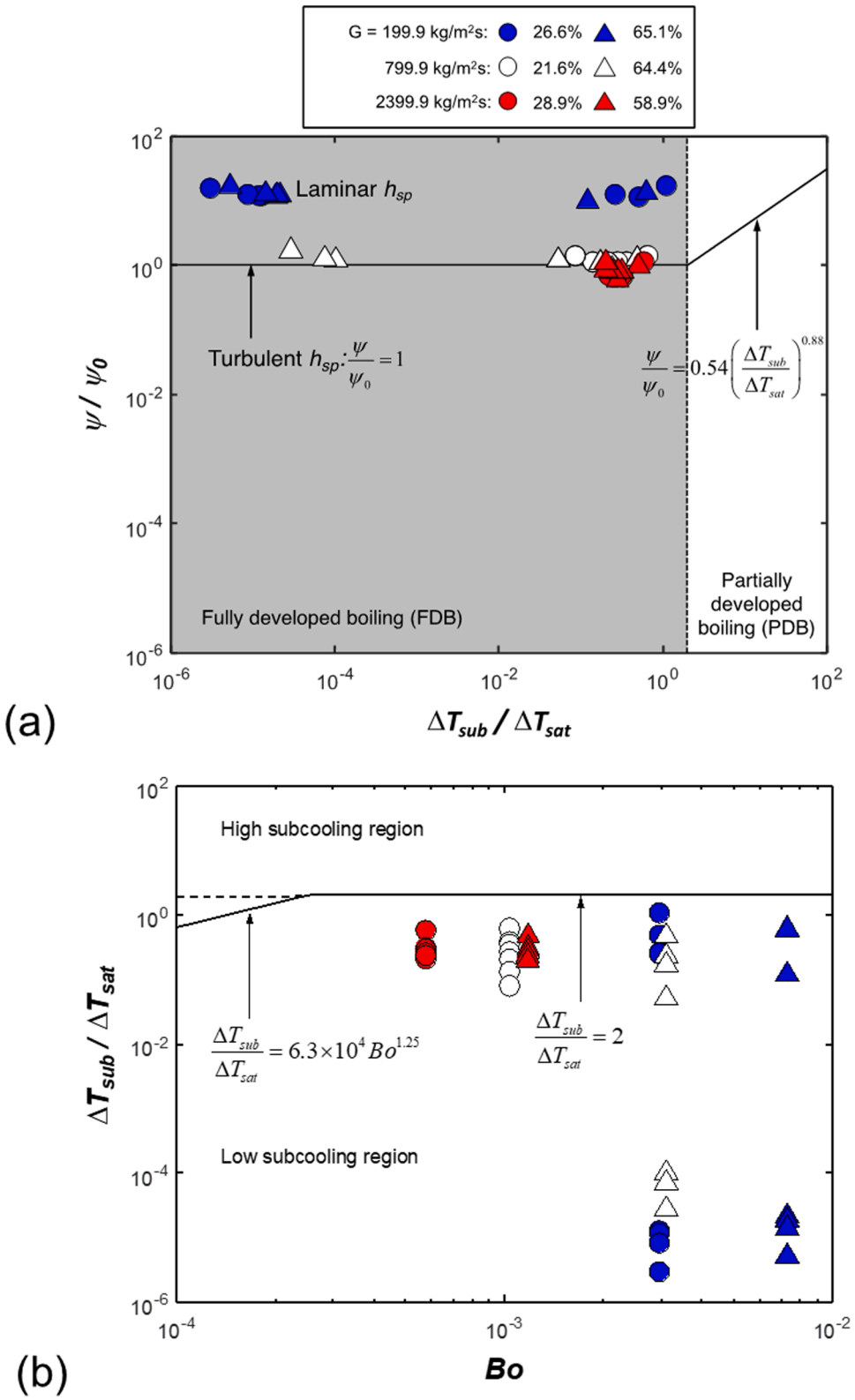

Fig. 4. Identification of boiling regime for low subcooled inlet conditions according to (a) ratio of dimensionless heat transfer rate, Ψ/Ψ_0 versus $\Delta T_{sub}/\Delta T_{sat}$, and (b) $\Delta T_{sub}/\Delta T_{sat}$ versus boiling number, Bo.

Unlike highly subcooled flow boiling, low subcooled flow boiling rapidly transitions into FDB due to faster development of thermal boundary layer along the heated wall upstream, which instigates quicker bubble growth and bubble departure. Data points evaluated in this study are mapped in two types of plots proposed by Mohammed and Shah [42] to determine dominant boiling regimes and to identify the transition from PDB to FDB. These plots demarcate PDB and FDB via magnitudes of the following dimensionless parameters:

$$\frac{\psi}{\psi_0} = \frac{q''/\left[h_{sp}\left(T_{w,b} - T_{sat}\right)\right]}{\psi_0}, \tag{28}$$

$$\frac{\Delta T_{sub}}{\Delta T_{sat}} = \frac{T_{sat} - T_f}{T_{w,b} - T_{sat}}, \tag{29}$$

and

$$Bo = \frac{q''}{Gh_{fg}} \tag{30}$$

where ψ is the ratio of average heat flux q'' (defined as total electrical power supplied to the copper slabs divided by total wetted area of heating walls of the channel's cross-section, $2WL_h$) to single phase heat flux, ψ_0 is the value of ψ corresponding to zero wall superheat, and Bo is the Boiling number. More details should be referred to Mudawar et al. [27]. Fig. 4(a) suggests the entire data set considered in this study falls into the FDB region, regardless of other operating conditions. This implies both onset of nucleate boiling (ONB) and net vapor generation (NVG) conditions occur in close proximity to the inlet, upstream of the first thermocouple location along the heated wall. Notice that the laminar flow conditions yield higher values of ψ/ψ_0 for the case with the lowest mass velocity of $G = 199.9$ kg/m^2 s. Data investigated in the

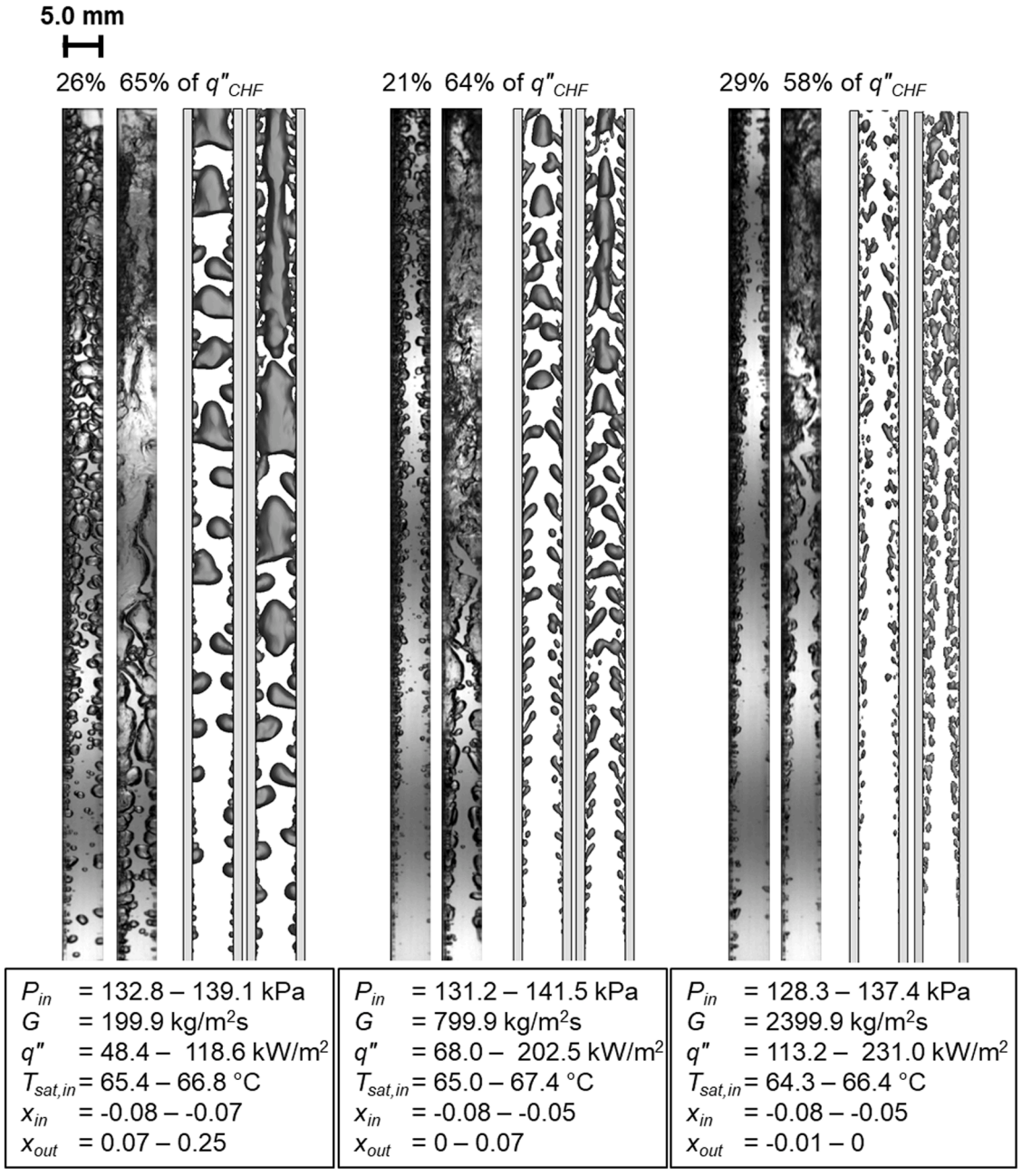

Fig. 5. Comparisons of experimentally captured flow visualizations with computational predictions for three mass velocities, each including two heat fluxes corresponding to similar percentages of CHF.

study can be further segregated by plotting $\Delta T_{sub}/\Delta T_{sat}$ versus Bo as seen in Fig. 4(b). Here too, for all the cases considered, FDB is shown to span the entire flow channel. Notably, data points for the maximum mass velocity of $G = 2399.9$ kg/m^2 s are clustered together, which indicates less variation of either wall temperature or fluid temperature along the channel.

4.2. Bubble behavior and hydrodynamic characteristics for low inlet subcooling

In microgravity, the absence of a body force results in the flow structure being governed by the combined effects of inertia and surface tension. In this regard, experimental measurements and video analysis are pivotal in evaluating the accuracy and efficacy of the 3-D CFD model. Fig. 5 depicts a comparison between high-speed video images obtained from representative flow boiling experiments conducted on the ISS and the predicted flow visualizations generated by the CFD model. Shown are comparisons for three distinct mass velocities and two CHF percentages. Both individual images from experiments and predictions exhibit instantaneous spatial tracking of interfacial behavior after a steady state is achieved. Wall heat flux, q'', is indicated as percentage of q''_{CHF}, the latter being the measured CHF value as listed in Table 1.

$$\%\ CHF = \frac{q''_{meas}}{q''_{CHF}} \times\ 100\ [\%] \tag{31}$$

As presented in Fig. 4, given the low inlet subcooling for all the cases considered, the high-speed images, as presented in Fig. 5, depict the rapid transition of the boiling regime from PDB to FDB within the upstream section of the channel close to the inlet. Close examination of the video images and the flow visualizations predicted by the CFD model in Fig. 5 reveals several important details regarding axial development of the interfacial structure. The simulation results are obtained after reaching a steady state and depict a monotonic increase in void fraction with an increase in heat flux for each mass velocity, ultimately leading to substantial vapor accumulation in the channel's downstream region. For the lowest mass velocity of $G = 199.9$ kg/m^2 s, the initiation of bubble nucleation occurs near the leading edge of the channel and is followed by subsequent bubble growth as the bubbles slide along the heated wall. At 26% CHF, as the void fraction along the channel increases, larger bubbles are detached from the heated wall and merge to form even larger bubbles. The migrating bubbles do not vanish or considerably decrease in size due to the weak condensation effect of low subcooled flow boiling. Farther downstream, both the video images and CFD visualization show the flow channel becomes densely packed due to coalescence of bubbles emerging from the opposite walls while, near the outlet, the flow channel is densely packed with large oblong vapor structures. At 65% CHF, the CFD model accurately captures the flow pattern observed in the experiment with large oblong vapor bubbles appearing at an earlier axial location compared to the lower heat flux case. Furthermore, and interestingly, the model is able to simulate nucleating bubbles in the liquid film surrounding the thick vapor core far downstream under the same operating conditions. Note that the ability of the CFD model to capture bubble nucleation in the liquid film ultimately leverages accurate prediction of wall temperature as will be discussed in detail in later sections.

For the intermediate mass velocity of $G = 799.9$ kg/m^2 s, bubble size from both experiment and CFD visualization becomes smaller, and bubble departure is enhanced due to the intensified interfacial shear and drag, two effects that are purposely incorporated in the present CFD model. Increasing heat flux induces more vapor generation along the channel, leading to formation of both large oblong bubbles and a rather continuous vapor core downstream, as observed at 64% CHF. However, when compared to the case with similar heat flux percentage but lower mass velocity, the predicted vapor core is thinner and shorter, highlighting the improved performance of the present CFD model in addressing the effects of flow inertia.

For the highest mass velocity of $G = 2399$ kg/m^2 s, the CFD model presents certain limitations in predicting accurate two-phase flow structure. The simulations predict small to large discrete bubbles mostly detached from the wall while the experiments show the formation of large oblong vapor structures remaining attached to the heated wall. Those differences will be shown later to cause deviations between predicted and measured wall temperatures for the highest mass velocity.

More details of the dynamic behavior of flow boiling are illustrated

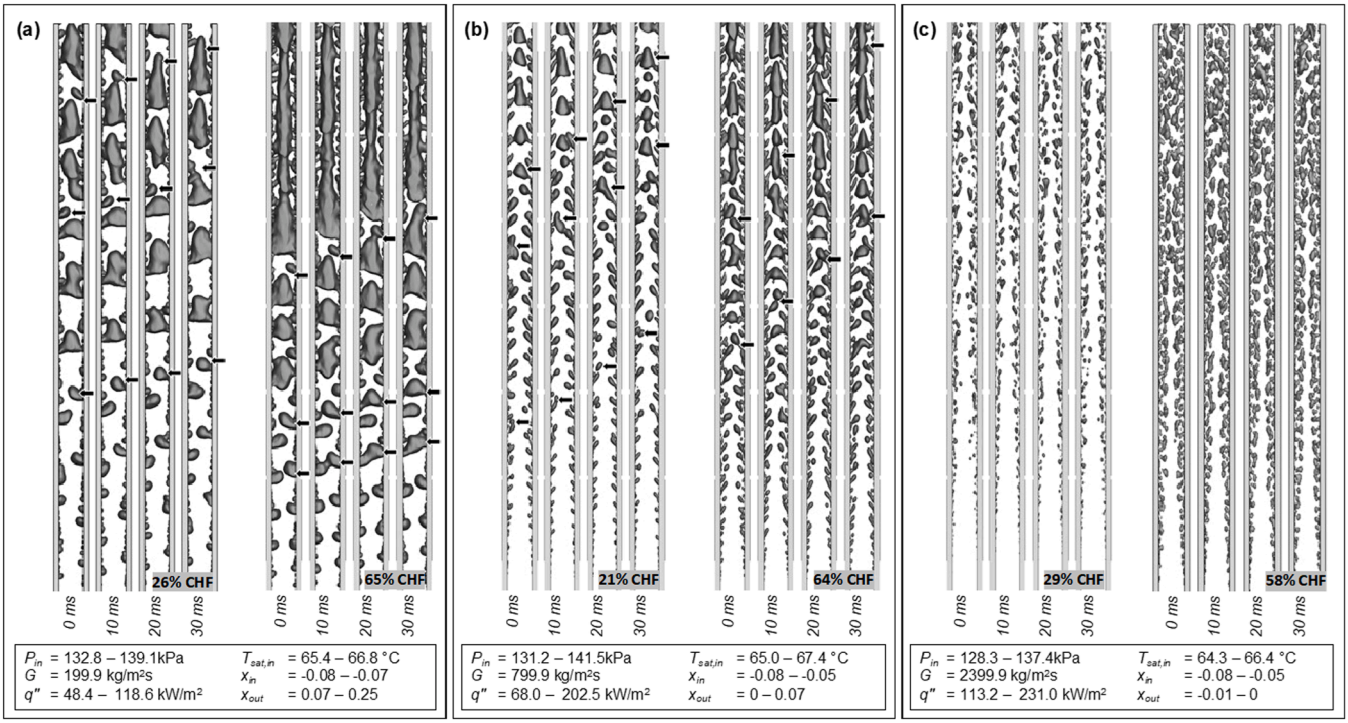

Fig. 6. Transient flow patterns from predictions of 3D computational model for G = (a) 199.9, (b) 799.9, and (c) 2399.9 kg/m^{2}s.

by sequential images captured from the simulations, which are shown in Fig. 6(a)–(c), wherein individual images in each sequence are separated by 10 ms. Shown for each of the mass velocities of $G = 199.9$, 799.9, and 2399.9 kg/m^2 s are visualizations for heat fluxes corresponding to around 20% and 60% CHF. The exact values of operating conditions including the heat fluxes are indicated in Fig. 6(a)–(c).

In Fig. 6(a), for $G = 199.9$ kg/m^2 s and 26% CHF, bubble nucleation commences near to the leading edge of the channel. With time, the bubbles slide along the heated wall, merging with the foregoing bubbles and increasing in size. It is noteworthy that in zero gravity, where there is no body force aiding bubble lift-off, the residence time of the bubbles on the heated wall is longer compared to that under terrestrial gravity. Nevertheless, as the bubbles grow, they experience a lift-off process promoted by interfacial shear and drag, both of which are induced by the velocity difference between the phases. The CFD model simulates the occurrence of bubble necking phenomena, where the induced shear lift force pushes the bubble away from the heated wall while the surface tension minimizes the interface surface area, as indicated by arrows in the middle of the channel. Departed and migrated bubbles coalesce with each other and produce large oblong vapor structures in the core. As these structures flow downstream, they continue to grow in size and length by engulfing nearby bubbles or absorbing bubbles attached to the heated wall, as indicated by arrows in the figure. Towards the end of the flow channel, the vapor structures agglomerate and densely pack the cross-section, intermittently making contact with both walls. At higher heat flux of 65% CHF, the flow development follows a similar pattern, but with a faster increase in void fraction. Downstream, oblong vapor structures coalesce to form a thick, elongated vapor core, while the remaining liquid flows in the periphery, forming a liquid film around the channel. Kharangate et al. [43] performed an experiment with FC-72 horizontal flow boiling using a rectangular channel and visualized bubble nucleation and vapor film formation along with bubble nucleation within a similar liquid film with a high-speed camera. The present CFD model demonstrate the ability to simulate active boiling within the liquid film, as shown in the downstream region of Fig. 6(a).

In Fig. 6(b), with an increase in the mass velocity to $G = 799$ kg/m^2 s, simulated flow regimes are distinctly different to those for the lower mass velocity. The intensified interfacial shear and drag, resulting from the increased flow inertia, ultimately lead to earlier bubble departure and reduced residence time on the heated wall. Consequently, the bubbles have less time to expand via phase change, resulting in significantly smaller bubble sizes at higher mass velocities. Here, the bubbles tend to stay close to the walls. This is because: (1) ability of the liquid to maintain its subcooling is considerable at higher mass flow rates, (2) bubble growth is limited within the thin thermal wall boundary layers, and (3) high inertia of the liquid prevents tiny bubbles from moving toward the bulk region. At 21% CHF, several different examples of bubble growth by coalescence are captured at three different axial locations. First, in the upstream region, strong shear induced by high flow inertia causes a captured bubble to detach from the heated wall and stretch in the flow direction. However, the detached bubble soon reattaches to a neighboring bubble on the heated wall, leading to coalescence into a larger bubble formation. The observed detaching bubble behavior can also be explained via the bubble breakup process, as revealed by Li et al. [39], where bubble transport and breakup of venturi mixture flow were successfully captured using coupled VOF and LES models. They demonstrated the capability of VOF in predicting bubble breakup phenomena and provided an explanation for the breakup mechanism. The VOF model's breakup mechanism relies on multiple contributing factors: Kelvin-Helmholtz instability, which causes bubbles to detach from the gas film, Rayleigh–Taylor instability, which induces the deformation of detached bubbles, viscous shear force, which reinforces the interfacial instability during the breakup process, and, finally, turbulent fluctuations and collisions, which play a role in the shattering of bubbles. These findings shed light on the underlying mechanisms behind the observed detaching bubble behavior from the CLSVOF model of the present study. Second, in the middle of the channel, a large oblong bubble lifts off from the wall and migrates towards the core. As it migrates, the oblong vapor structure attracts and pinches off a chunk of vapor from neighboring bubbles, eventually merging to form an even longer bubble. Lastly, in the downstream region, small bubbles on the heated walls are observed to be swept and absorbed by a central rather continuous long vapor core. At 64% CHF, similar bubble growth patterns through coalescence are observed, but with a further transition into more chaotic structure. The larger size of bubbles is attributed to the more aggressive bubble nucleation and higher interfacial evaporation rate caused by the increased wall superheat, leading to enhanced bubble detachment. Large bubbles migrating towards the center of the channel collide and coalesce with each other, producing larger and longer central bubbles as indicated by the arrows in the figure. Moreover, further downstream, elongated bubbles at the center core connect, leading to regime transition into annular-like flow. Note that impact of the bubble collision dispersion force, which is very pronounced for clusters of small, dispersed bubbles diminishes appreciably for larger bubbles [14].

On the other hand, for Fig. 6(c) with the highest mass velocity of $G = 2399.9$ kg/m^2 s, the predicted flow patterns are predominantly bubbly flow along the entire heated length despite the increasing vapor concentration at the higher heat flux, and, for both heat fluxes, a significant portion of the channel's cross section is occupied by liquid and discrete bubbles are constrained near the walls.

Fig. 7 shows isometric views of the predicted flow pattern for $G = 199.9$ kg/m^2 s and 26.6% CHF. Magnified views for upstream, middle, and downstream sections are provided to clearly manifest the simulated interfacial structure, key among which is the morphology of vapor bubble bases and dry patches. In Fig. 7(a), growing small bubbles are attached to the heated walls, forming bubble bases identified by the contact line. As indicated with arrows, there are instances where fully dried small patches are present among the bubble bases. Similar configurations are presented for the middle section in Fig. 7(b) and the downstream section in Fig. 7(c). Notably, for all three sections, the areas occupied by both bubble bases and dry patches has a small footprint as a percentage of the heated wall surface area, indicating that nucleated bubbles detach easily from the heated wall before they excessively expand in volume. Subsequently, the detached bubbles merge with each other to form larger oblong bubbles or vapor columns along the core of the channel, as shown in Fig. 7(b) and (c). Consequently, the contribution of microlayer heat transfer to bubble growth and overall flow boiling performance is anticipated to be quite small. In contrast, in the context of mini/micro-channel flow boiling, the microlayer effect is far more pronounced. A recent numerical study by Chen et al. [44] on mini-channel water flow boiling demonstrated that due to the higher surface tension of water when compared to those of nPFH, nucleated bubbles tend to stay attached to the heated wall for a longer duration and, because of the confinement effects of the small channel, undergo axial expansion, resulting in the formation of elongated bubbles that congest the flow channel. These elongated bubbles were observed to create wider bases for the bubbles and broader dry patches, which is unlike the observations made in the present study. As a result, the microlayer heat transfer mechanism is expected to be more crucial in mini/micro-channel flow boiling scenarios, leading to distinctive bubble dynamics compared to those observed in the current study.

Fig. 8 displays transverse void fraction profiles at different axial locations along the channel for each of the three mass velocities. Time-averages for the void fraction are achieved over a period of one second. The symmetries in the inlet velocity profile and heat flux applied to the heated walls are reflected in the vapor void fraction predictions. The largest variation of vapor generation is observed at the lowest mass velocity as confirmed both from predicted and experimentally captured flow visualizations in Fig. 5. For the lowest mass velocity of $G = 199.9$ kg/m^2 s, at the axial location of $z = 5.4$ mm, the void fraction profiles for both heat fluxes exhibit zero value in the core, but a steep increase

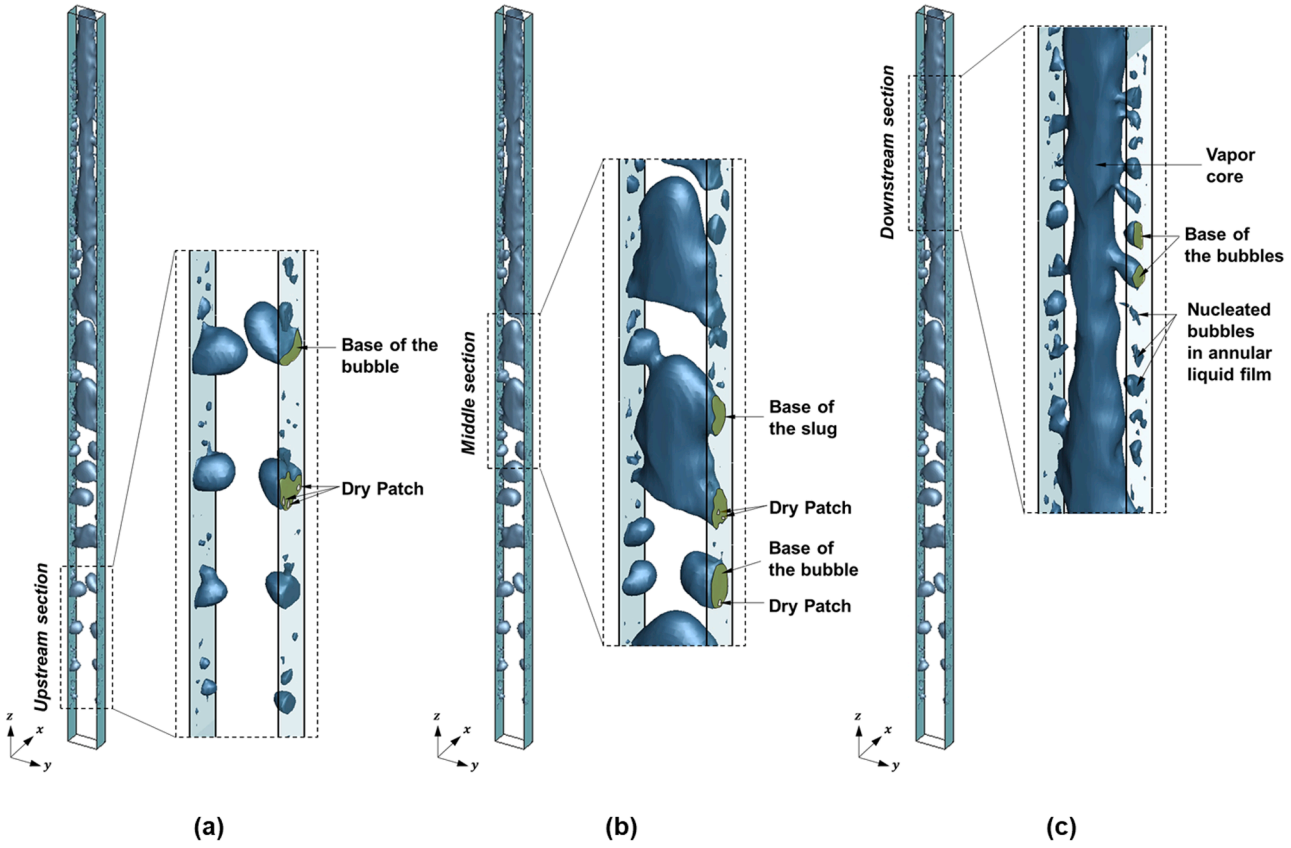

Fig. 7. Predicted flow structure along the flow channel highlighting the small footprint of bubble bases and dry patches for G = 199.9 kg/m^{2}s and 26.6% CHF in (a) upstream section, (b) middle section, and (c) downstream section.

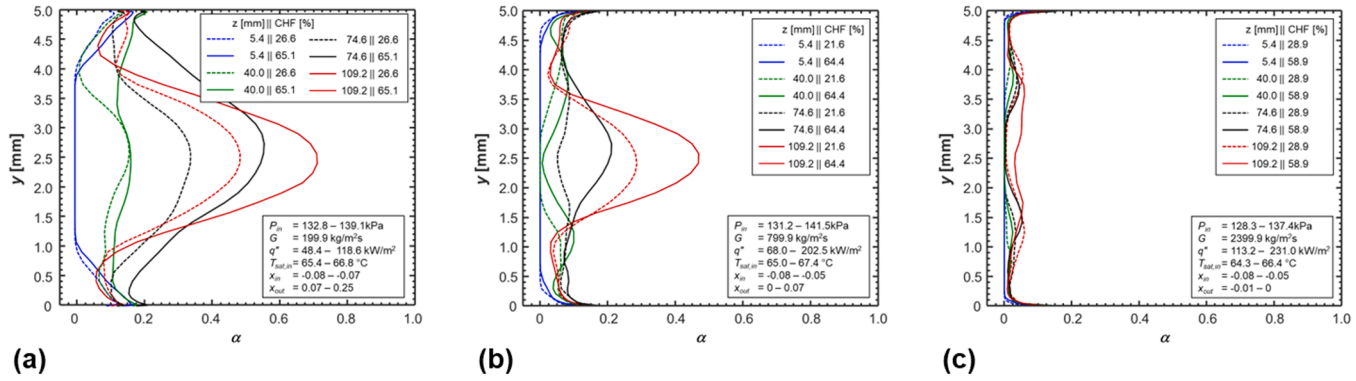

Fig. 8. Time-averaged local void fraction (α) profiles between the heated walls for (a) G = 199.9 kg/m^{2}s, 21.6% CHF and 65.1% CHF, (b) G = 799.9 kg/m^{2}s, 21.6% CHF and 64.4% CHF, and (c) G = 2399.9 kg/m^{2}s, 28.9% CHF and 58.9% CHF.

towards the heated walls. Despite the low subcooling at the inlet, newly nucleated small bubbles cannot penetrate into the central core due to the condensation effect in the bulk liquid. As they depart from the walls, they recondense back to liquid. The void fraction profiles evolve into a bell-shaped profile due to bubble growth and detachment from the heated wall, and subsequent agglomeration at the core. At far downstream of z = 109.2 mm, peaks of the profiles for both heat fluxes are observed at the center of the channel, indicating the presence of the large oblong bubbles in the same region. The slight increase towards the walls suggests persisting bubble nucleation within the surrounding liquid film. Under higher mass velocity, as witnessed from Fig. 6(b), (c), vapor concentration significantly decreases. The trend is also captured in the void fraction profile in Fig. 8(b) and (c), accordingly. In Fig. 8(b), for mass velocity of G = 799.9 kg/m^2 s, despite the presence of nearly symmetrical bell shape profile, the peak values of void fraction at the most downstream location for both heat fluxes are much smaller than those in Fig. 8(a). Notice it is not only the peak value of void fraction but also width of the bell shape profile which dictates the thickness of the vapor core; it is much smaller in Fig. 8(b) than in Fig. 8(a). Both of these trends are quantitatively describing the effect of increasing mass velocity in the large oblong bubble regime. The effect of excessive increase of mass velocity is echoed in void fraction profiles shown in Fig. 8(c). For the highest mass velocity of G = 2399.9 kg/m^2 s, the void profile exhibits near-wall peaks with a near-zero value throughout much of the core, which is attributed to the greater sensible energy content in the subcooled liquid at high mass velocities. Moreover, the confinement of the bubble layer to the wall region is due to the increased liquid inertia at the highest mass velocity.

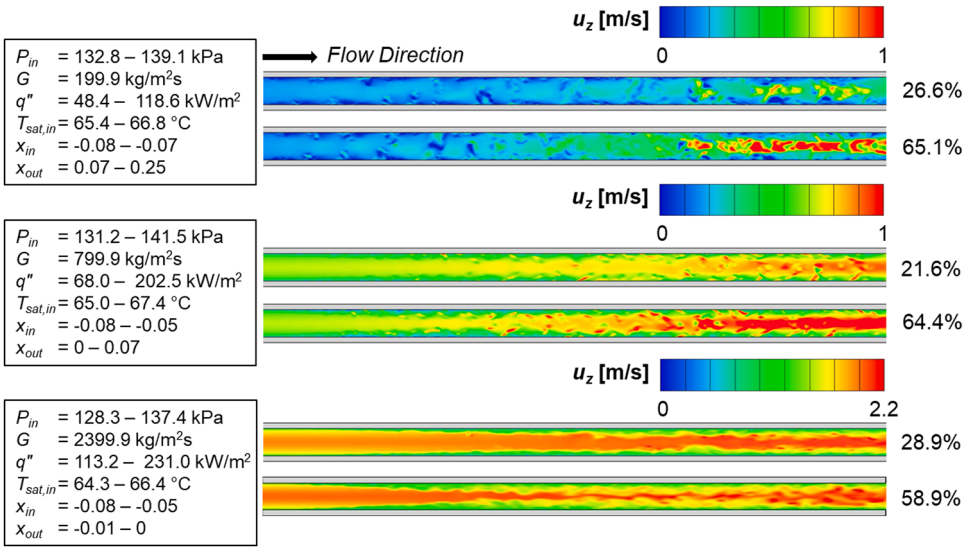

Fig. 9. Predicted velocity (u_z) contours along flow direction for G = 199.9, 799.9, and 2399.9 kg/m^{2}s.

Acceleration of fluid flow along the boiling channel is strongly interrelated with two-phase flow structure and transition of flow regime. In Fig. 9, velocity field contours are shown for the three different mass velocities and two different heat flux percentages. For the lowest mass velocity of G = 199.9 kg/m^2 s and 26.6% CHF, for the inlet region, the colormap is predominantly blue in color indicating minimal change of velocity along with limited velocity field distortions confined to the near wall region. Starting from the middle of the channel, as flow regime transitions from one containing small bubbles to another comprised of larger, oblong bubbles, the colormap depicts not only the accelerating fluid velocity but also intensifying flow distortions within the velocity field. This distortion, which accounts for fluid mixing and turbulence induced by bubble movements and fusion process, accounts for enhanced thermal dissipation and heat transfer performance of two-phase flow when compared to that of single-phase flow. As heat flux is increased to 65.1% CHF, the flow acceleration exacerbates, and velocity field becomes more chaotic, due to the emergence of large oblong bubbles and an elongated vapor core downstream of the channel, as confirmed from flow visualizations in Figs. 5 and 6. Note that fluid velocity at the core of the channel is much higher than at the near-wall region, which highlights velocity difference between vapor core and liquid film. By employing the same colormap scale from the case of G = 199.9 kg/m^2 s onto G = 799.9 kg/m^2 s, it is possible to graphically compare the effect of increased mass velocity on two-phase flow field characteristics. First, obviously, higher mass velocity induces higher flow velocity by which interfacial shear and drag are strengthened and causes earlier bubble departure to result in smaller size bubbles. Second, due to the smaller bubble size and less active bubble migration towards the core, flow field distortion is less severe. Note that this qualitative understanding of velocity field distortions will be quantitatively presented below as velocity profiles in Fig. 10. The simulated velocity contours for the highest mass velocity of G = 2399.9 kg/m^2 s show diminished difference between the two heat flux percentages when compared to the lower mass velocity cases, mainly due to excessive flow inertia causing flow regime to be predominantly consisting of small bubbles throughout the channel which precipitates attenuated flow distortions.

The transverse fluid velocity profiles for the three mass velocities, each at four different axial locations along the channel and the two different heat flux percentages, are shown in Fig. 10. Time averages for the fluid velocities are achieved over a period of one second. Fig 10(a) shows streamwise velocity profiles for the lowest mass velocity of G = 199.9 kg/m^2 s. At the axial location of z = 5.4 mm, regardless of heat flux condition, velocity profiles show minimum y-direction distortion due to the small size of bubbles remaining attached to the heated walls. At farther axial locations of z = 40.0 and 74.6 mm, fluid velocity difference between the two heat flux percentages becomes larger as greater amount of vapor is generated and accumulated at the higher heat flux condition. Evidently, greater void fraction at the higher heat flux implies vigorous bubble detachment, migration, and coalescence, which all

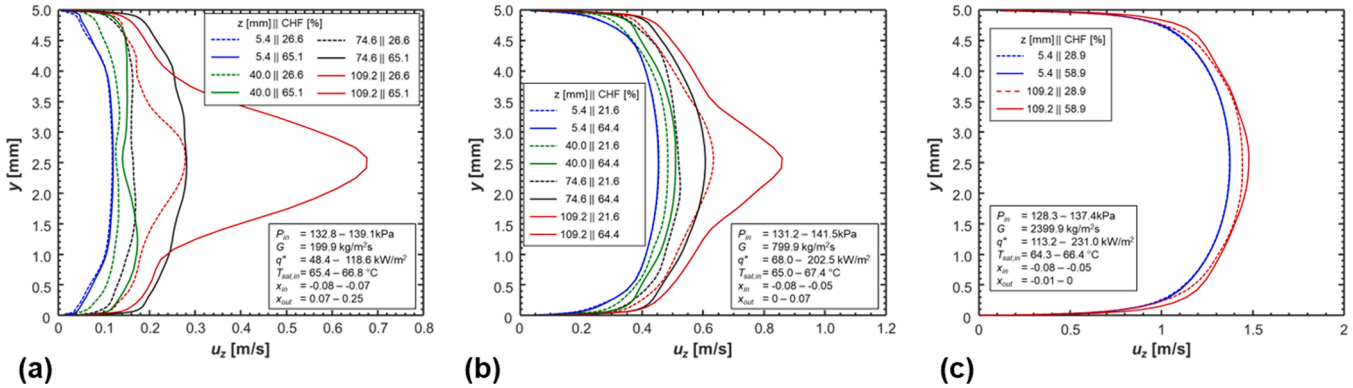

Fig. 10. Time-averaged local streamwise velocity (u_z) profiles between the heated walls for (a) G = 199.9 kg/m^{2}s, 21.6% CHF and 65.1% CHF, (b) G = 799.9 kg/m^{2}s, 21.6% CHF and 64.4% CHF, and (c) G = 2399.9 kg/m^{2}s, 28.9% CHF and 58.9% CHF.

together support increasing severity of flow distortion. Farther downstream of the channel, specifically at $z = 109.2$ mm, the formation of large oblong vapor structures and elongated thick vapor core at 26.6% and 65.1% CHF, respectively, engenders distinct maxima within the velocity profiles at the channel core. Notably, for the higher mass velocities of $G = 799.9$ and 2399.9 kg/m^2 s, in Fig. 10(b) and (c), respectively, two obvious differences from Fig. 10(a) trends are readily apparent. First, fluid velocity profiles present increased velocity when compared to Fig. 10(a), which leads to the strengthening of interfacial shear and drag, resulting in earlier bubble departure and smaller void fraction. Second, more importantly, because of smaller void fraction (see Fig. 8(b)), both the profile distortions and flow acceleration effects are attenuated. Notice the clean bell shape profile without minimal flow distortion at all axial locations for the highest mass velocity of $G =$ 2399.9 kg/m^2 s.

4.3. Flow boiling heat transfer characteristics

Based on the computed two-phase flow structure and velocity field, various heat transfer parameters are evaluated to better understand two-phase heat transfer characteristics which are difficult to measure or analyze experimentally.

Fig. 11(a) shows fluid mixture temperature, T_m, in the heated portion of the flow channel for the six test cases. These contour plots are captured from the center ($y - z$) plane at $x = 0$. The operating conditions for each case are listed in the insets next to each figure, which are identical to those in Fig. 9. Notice how all six conditions involve low inlet subcooling with saturation temperatures varying between 64.3 and 67.4 °C. At the lowest mass velocity of $G = 199.9$ kg/m^2 s and 26.6% CHF, the inlet region of the channel exhibits predominantly blue color, indicating subcooled fluid temperature with the emerging thermal boundary layers being confined to the near-wall region. The colormap shows gradual development of thermal boundary layers as bubbles nucleate and grow in size along the flow channel. The temperature field in the middle to downstream region of the channel demonstrates a gradual increase in temperature as a result of thermal energy transport via bubble departure and migration towards the core. This leads to an almost fully saturated fluid temperature, as shown by the contour plots. Note that thermal energy transport is reinforced with increasing turbulent mixing in the downstream region, which is induced by accelerating fluid velocity and intensifying flow distortion, as also confirmed from the fluid velocity field in Fig. 9. With an increase in heat flux to 65.1% CHF, the fluid temperature increases rapidly, indicated by the earlier transition of color in the temperature field contour, accompanied by more vigorously expanding thermal boundary layers. Further downstream, the fluid mixture temperature rises above the saturation temperature in the near-wall region due to the presence of superheated vapor, while the steady-state wall temperature is maintained by continuous liquid replenishment onto the heated wall. Extrapolating the trend, if imposed with higher heat flux near to CHF, it can be expected that the mixture temperature near the heated wall will increase even more due to the development of vapor layers. This would effectively insulate the heated wall from colder liquid contact, eventually leading to an unsteady excursion of the wall temperature. Evaluated with the same colormap scale among the cases, it is possible to graphically understand the effect of increased mass velocity on temperature field characteristics. The colormap of higher mass velocity cases depicts less diffusive and slower transition of color along the boiling channel when compared to the cases with the lowest mass velocity. This implies that subcooled liquid core under high mass velocity can further penetrate into the downstream region due to less active bubble migration towards core, and less severe flow distortion as can be deduced from Figs. 6 and 9.

Fig. 11(b) presents wall temperature contours for three different mass velocities, each with two different heat flux conditions. Each contour plot also captures the predicted flow pattern. From Fig. 11(b), a common trend of wall temperature variation can be observed across all cases, with the colormap displaying an almost constant wall temperature that slightly and gradually decreases towards both the inlet and outlet. Furthermore, for all three mass velocities, wall temperatures are higher for the higher heat flux percentage than the lower. For the higher heat flux percentage, the higher wall temperatures for the highest mass velocity followed by intermediate and the lowest are the outcome of higher absolute values of wall heat flux for the former, and not indicative of compromised heat transfer effectiveness with increasing mass velocity.

Fig. 12 shows cross-sectional profiles of computed fluid mixture temperature for mass velocities of $G = 199.9$, 799.9, and 2399.9 kg/m^2 s, each including profile trends for multiple axial locations and two heat flux percentages. Time averages for the fluid temperature are achieved over a period of one second after steady state. The temperature profiles

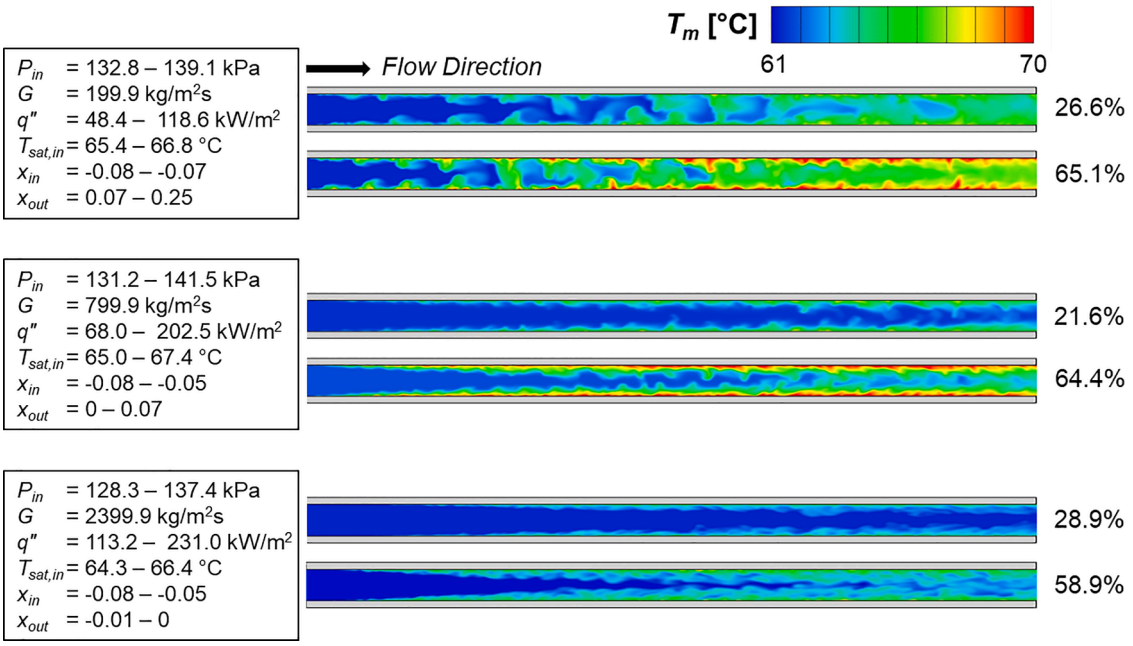

Fig. 11(a). Predicted mixture temperature (T_m) contours along flow direction for G = 199.9, 799.9, and 2399.9 kg/m^{2}s.

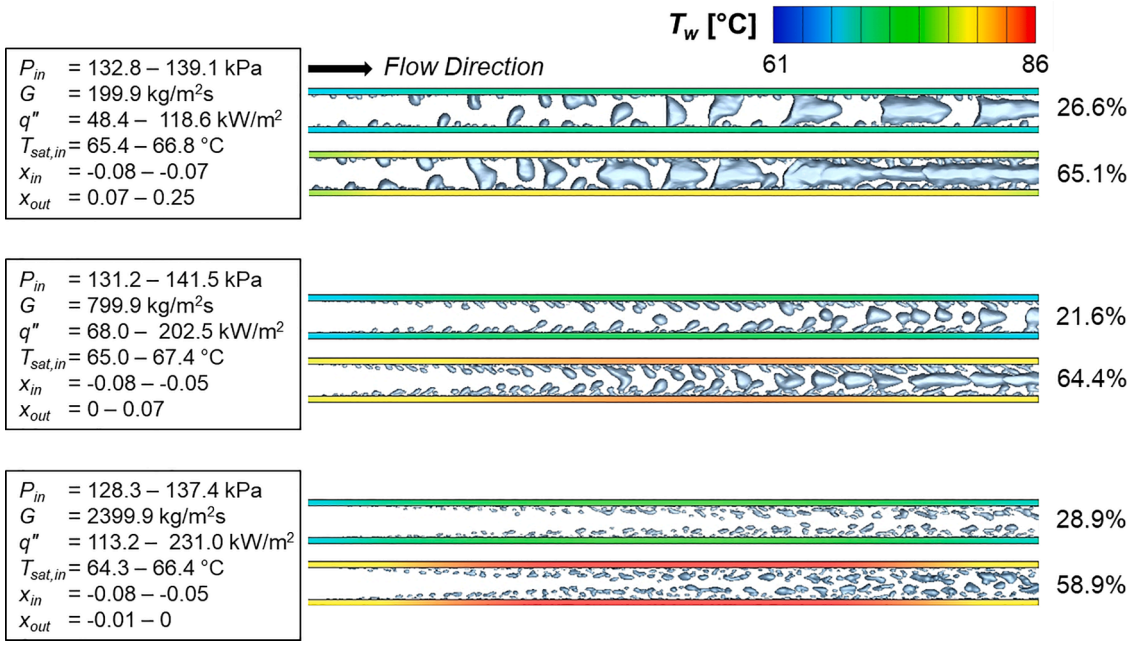

Fig. 11(b). Predicted wall temperature (T_w) contours and flow patterns along flow direction for G = 199.9, 799.9, and 2399.9 kg/m²s.

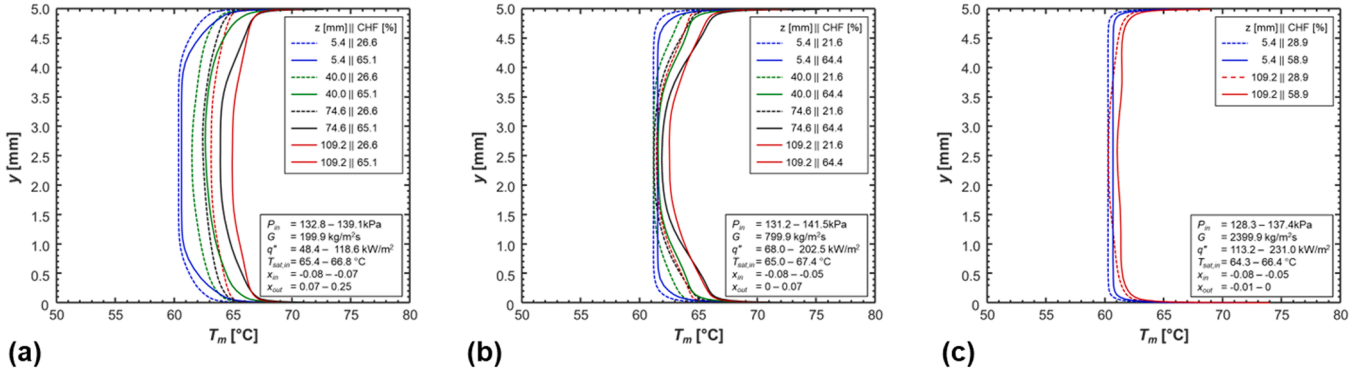

Fig. 12. Time-averaged local streamwise mixture temperature (T_m) profiles between the heated walls for (a) G = 199.9 kg/m²s, 21.6% CHF and 65.1% CHF, (b) G = 799.9 kg/m²s, 21.6% CHF and 64.4% CHF, and (c) G = 2399.9 kg/m²s, 28.9% CHF and 58.9% CHF.

commonly exhibit a concave shape with increasing temperature near the walls and colder bulk fluid in the central core, indicating the development of a thermal boundary layer near the walls. The axial increase of fluid temperature is attributed to development of the single-phase liquid thermal boundary layer, caused by diffusion and advection from the heated walls, for upstream locations with low wall heating. For downstream locations with high wall heating, the temperature rise is mainly induced by the migration and agglomeration of bubbles, resulting in an increase in the core temperature. For the lowest mass velocity of G = 199.9 kg/m² s, Fig. 12(a), concavity of the profiles is the largest out of all the presented cases, highlighting the effect of turbulent mixing induced by bubble growth, departure, migration, and coalescence, which are evaluated to be the most severe at the lowest mass velocity from Fig. 9. Notice the decreasing concavity with distance due to the significant increase of core temperature particularly for the lowest mass velocity case. Especially, under 65.1% CHF, predicted core temperature reaches T_{sat} at the downstream location of z = 109.2 mm, which well corresponds with positive outlet equilibrium quality, as noted in the figure. In Fig. 12(b), with the increased mass velocity of G = 799.9 kg/m² s, flatter temperature profiles are presented, implying thinner thermal boundary layers with thicker subcooled core fluid, mirroring the observations from the temperature field contours in Fig. 11. Here, the core temperature is maintained below saturation temperature throughout the axial locations, regardless of heat flux conditions, resulting in negative vapor qualities at the exit of the channel for both heat flux percentages. For the highest mass velocity of G = 2399.9 kg/m² s, Fig. 12(c), the changes in fluid temperature profile with heating and axial location are further attenuated, resulting in nearly uniform subcooled temperature along the cross-section of the channel.

Results earlier showed effectiveness of the CFD model in capturing detailed interfacial behavior along the channel. Another measure for the model effectiveness is ability to accurately predict (1) bulk fluid temperature and (2) heated wall temperature. Note that the two form the basis for calculating the heat transfer coefficient.

Fig. 13 compares axial variations of numerically computed and analytically calculated average fluid temperature, T_m, for the three mass velocities of G = 199.9, 799.9, and 2399.9 kg/m² s and two different heat flux percentages. Note that the numerically predicted mixture temperatures are area-weighted averages of cross-sectional fluid temperature at each axial location, while the analytically estimated fluid temperatures are based on inlet and outlet measured fluid temperatures and pressures. In order to retrieve area-weighted mixture temperature, iso-surfaces were defined within the fluid domain at multiple axial locations. Then the area-weighted averaging calculations were performed

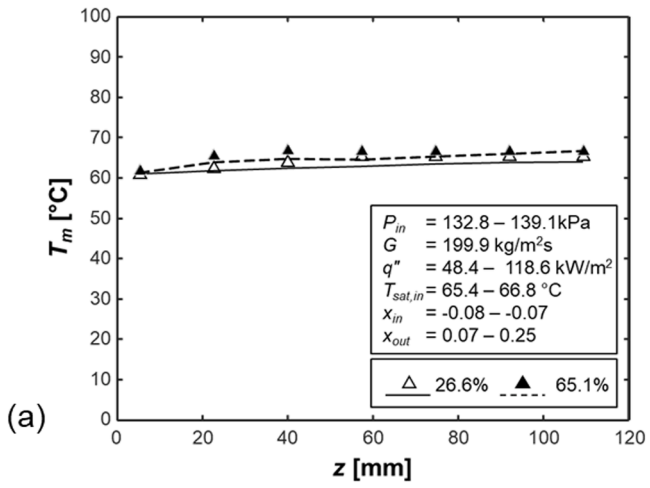

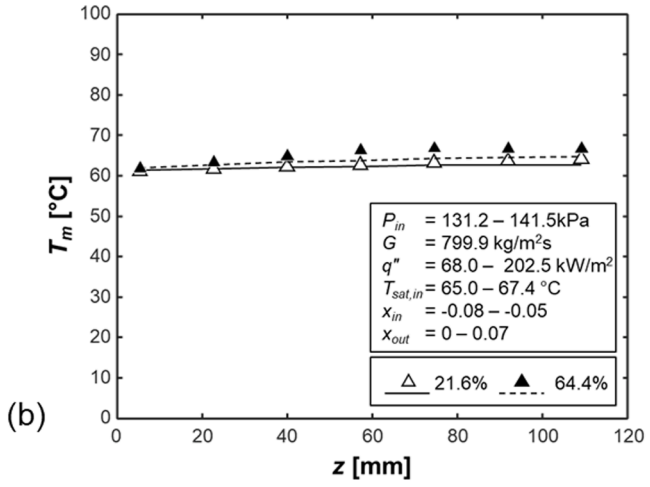

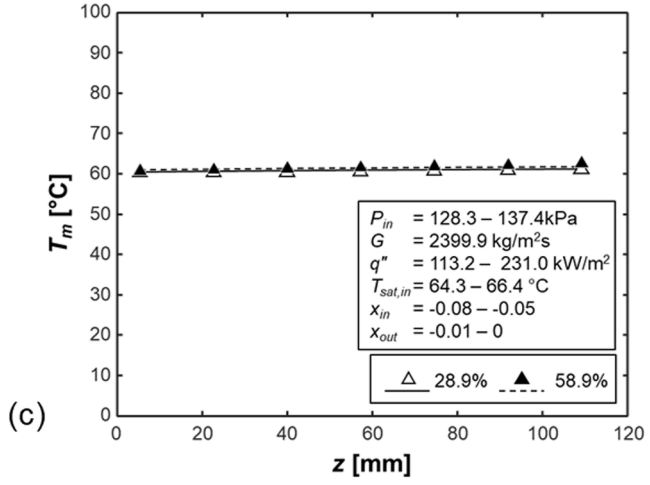

Fig. 13. Comparisons of measured and predicted axial variations of cross-sectional area-averaged mixture temperature (T_m) for (a) G = 199.9 kg/m^{2}s, 21.6% CHF and 65.1% CHF, (b) G = 799.9 kg/m^{2}s, 21.6% CHF and 64.4% CHF, and (c) G = 2399.9 kg/m^{2}s, 28.9% CHF and 58.9% CHF.

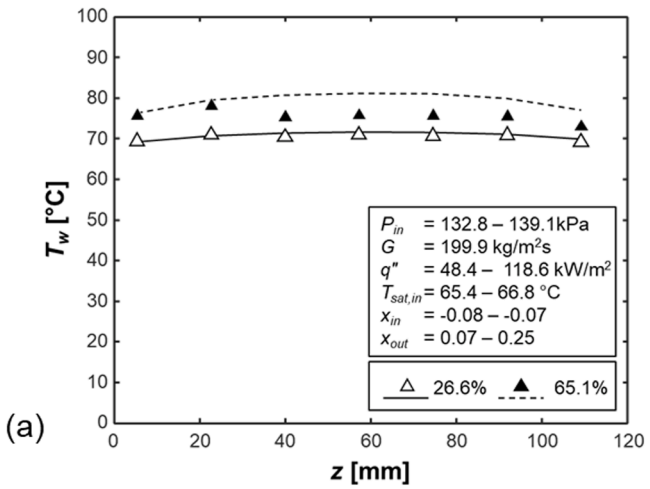

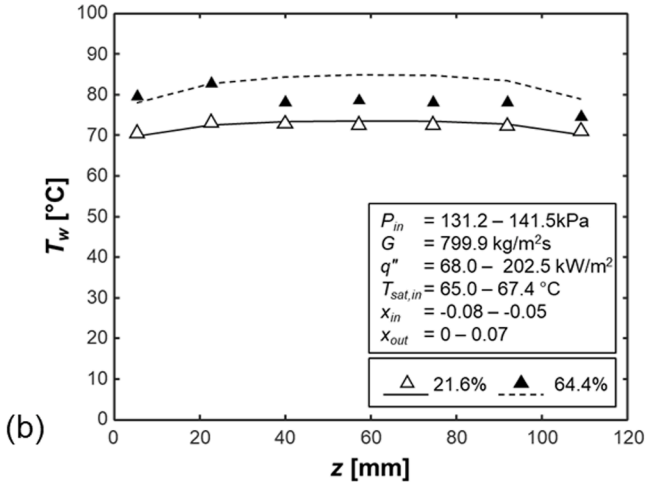

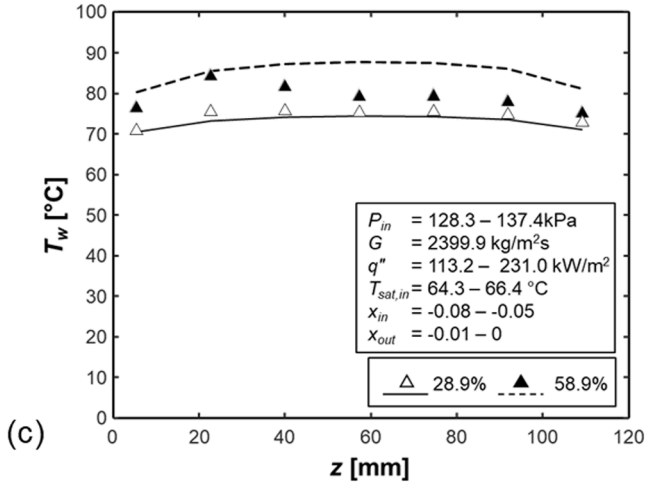

Fig. 14. Comparisons of measured and predicted axial variations of heated wall temperature (T_w) of six different flow boiling cases for (a) G = 199.9 kg/m^{2}s, 21.6% CHF and 65.1% CHF, (b) G = 799.9 kg/m^{2}s, 21.6% CHF and 64.4% CHF, and (c) G = 2399.9 kg/m^{2}s, 28.9% CHF and 58.9% CHF.

by FLUENT which computes the area-weighted average of a quantity by dividing the summation of the product of the mixture temperature and facet area by the total area of the surface [32]. Here, local pressure variation is assumed to be linear between measured inlet and outlet pressure. Calculation of fluid temperature upstream of the axial location of zero thermodynamic equilibrium quality, x_e, is based on simple sensible heat gain. Whereas, for downstream locations where $0 < x_e < 1$, local fluid temperature is set equal to saturation temperature corresponding to local pressure. Accordingly, the analytical axial temperature profile linearly increases until it reaches $x_e = 0$, which is then followed by nearly constant local saturation temperatures until the exit of the channel. In comparison, the numerically computed profiles show almost uniform but slowly increasing temperature curves, representing typical flow characteristics of low subcooled flow boiling where flow regime

rapidly transits from PDB to FDB then to saturated flow boiling, as identified in Fig. 4. Maximum deviation of 2.4 °C is detected from the case of the lowest mass velocity of $G = 199.9$ kg/m^2 s and 26.6% CHF at the axial location of $z = 57.3$ mm. The difference between the numerical and analytical fluid temperatures is a result of non-equilibrium effects that are captured by the CFD model. Overall, Fig. 13 shows good agreement between numerically computed and analytically calculated fluid temperatures, especially in the inlet and outlet regions, highlighting superior ability of the present CFD model in predicting the bulk fluid temperature.

Fig. 14 compares measured and predicted heated wall temperature variations along the channel for the three mass velocities and two heat flux percentages. The temperatures are measured experimentally by the thermocouples embedded into the copper slab at z = 5.4, 22.7, 40.0, 57.3, 74.6, 91.9, and 109.2 mm. The predicted temperatures are calculated within the solid cells at the exact depth of the thermocouple, then time-averaged for one second after steady state. For all six cases, both the measured and the predicted wall temperature curves show similar behavior: nearly constant wall temperature with slightly lower temperatures in the entrance and exit regions. The uniform wall temperature trend indicates nucleate boiling dominant heat transfer regime throughout most of the flow channel, which has been validated with flow visualizations in Figs. 5 and 6. The upstream lower wall temperatures are attributed to the development of thermal boundary layer where ineffective single-phase heat transfer dominates thermal energy transport process while two phase flow is still developing. Whereas the downstream lower temperatures are induced by enhanced heat transfer coefficient brought about by the flow acceleration due to the increased vapor void fraction in the exit region. Notice the ability of the CFD model to simulate the entrance and exit effects, replicating the experimental results. It can be observed from Fig. 14 that the predicted wall temperature curves show excellent agreement with the measured wall temperature curves for the cases corresponding to lower heat flux percentages for each of the three mass velocities, highlighting the superior predictive capability of the present CFD model with the CLSVOF method for flow boiling channels. It should also be recognized that, with inclusion of additional force terms such as shear lift force and bubble collision dispersion force in the CLSVOF model, under-represented bubble-to-bubble interactions such as dispersion due to bubble collision are counterpoised, enhancing accuracy of the wall temperature predictions [14].

For the cases with higher heat flux percentage at each mass velocity condition larger deviations are detected, with the maximum deviation of 8.5 °C corresponding to $G = 2399.9$ kg/m^2 s, 58.9% CHF, and axial location of $z = 57.3$ mm. As mentioned earlier, the accuracy of a CFD model in predicting heat transfer parameters depends on the accuracy of predicting interfacial flow pattern. Recall the comparison results from Fig. 5 for the highest mass velocity cases where the numerically predicted void fraction was lesser than what has been captured from experiment. The CFD model predicted a bubbly flow with small to large discrete bubbles, whereas in the experiment, large oblong vapor structures were formed and resided on or near to the heated wall. The underprediction of vapor void fraction along the flow channel in the CFD model leads to reduced efficiency of heat dissipation from the heated wall, resulting in higher predicted wall temperature compared to the measured wall temperature. Another possible factor for the deviation is related to details of bubble-induced turbulence, which stems from inherent limitations of the numerical and mathematical algorithms when computing liquid velocities around bubbles and the use of volume fraction averaged physical properties at mixture cells to avoid sharp discontinuities across the interface that cannot be numerically differentiated. Overall, despite these deviations, Fig. 14 exhibited fairly good accuracy of the current CFD model in predicting heated wall temperatures.

Fig. 15 demonstrates the impact of inlet subcooling on microgravity flow boiling performance for the three different mass velocities of G = 199.9, 799.9, and 2399.9 kg/m^2 s and two heat fluxes of approximately 20% and 60% CHF. By combining the results of highly subcooled inlet cases from Mudawar et al. [38] with the low subcooled inlet cases of the current study, a common observation is that measured wall temperatures are higher for near-saturated inlet cases, regardless of mass velocity or heat flux percentage. The predicted wall temperature profiles highlight the ability of the CFD model to accurately track the effects of inlet subcooling. Indeed, the comprehensive evaluation provided in the present study lends strong support for the CFD model's ability to simulate microgravity flow boiling, encompassing a wide range of operating conditions, including variations not only of mass velocity and heat flux, but also inlet subcooling. By successfully capturing the flow boiling behavior under diverse scenarios, the CFD model demonstrates its capability to effectively tackle the complexities of microgravity flow boiling across a broad spectrum of conditions. Nonetheless, future work might shed useful additional light on the model's capabilities in two important areas: (i) mini-micro-channel flow boiling [45], and (ii) flow boiling instabilities [46].

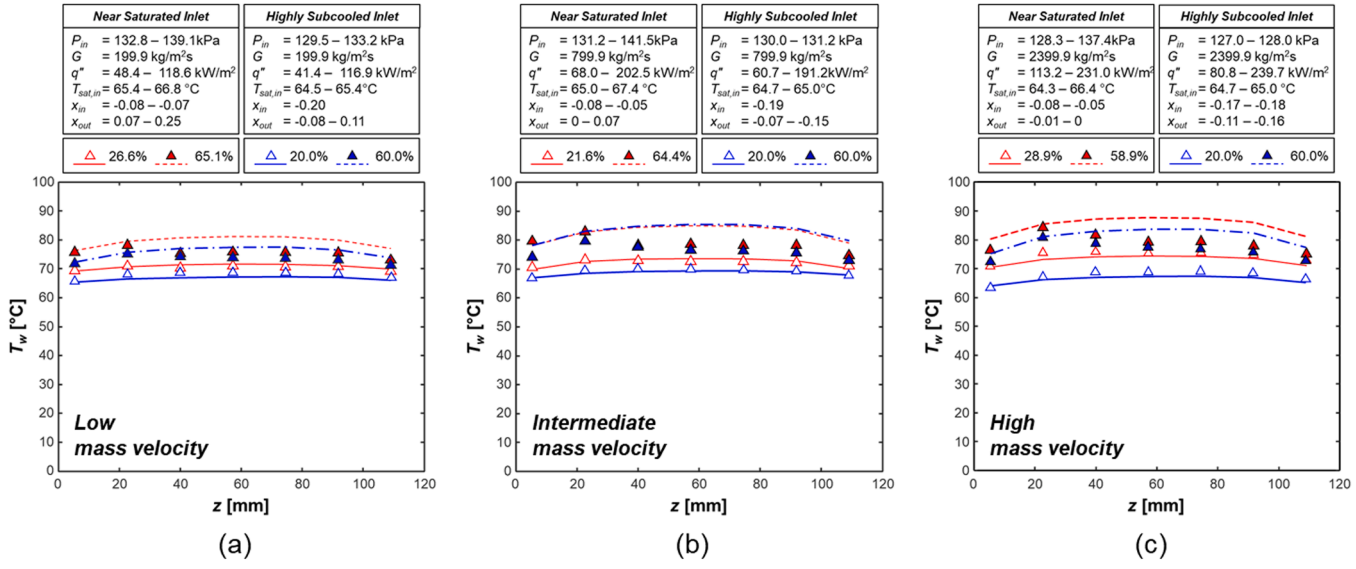

Fig. 15. Impact of inlet subcooling on measured and predicted axial variations of heated wall temperature (T_w) for (a) low mass velocity (G = 199.9 kg/m^{2}s), (b) intermediate mass velocity (G = 799.9 kg/m^{2}s), and (c) high mass velocity (G = 2399.9 kg/m^{2}s), each with two heat fluxes of approximately 20% CHF and 60% CHF.

Revisiting and reiterating the criteria for evaluating performance of a flow boiling model, the current CFD model has been proven capable of (1) precisely computing axial variation of bulk fluid temperature, and (2) computing heated wall temperature with fairly good accuracy, which validates the possibility of the present CFD model to be used as a reliable alternative for design of practical two-phase thermal systems in space applications (Fig. 15).

5. Conclusions

The present study focused on the use of Computational Fluid Dynamics (CFD) to predict low subcooled flow boiling of n-PFH in microgravity. The employed computational methodology provided detailed 3-D projections of interfacial behavior and heat transfer characteristics along a rectangular channel that is heated along two opposing walls. The adopted methodology is based on the CLSVOF model, which is combined with appropriate phase change and turbulence models. The model is further modified and enhanced by incorporating additional forces attributed to surface tension, drag, shear-lift on bubbles, and bubble collision dispersion. Furthermore, the model accounts for conjugate heat transfer along the heated walls. The validation of the CFD model is established by comparing the predictions to experimental wall temperature measurements and high-speed video images obtained from experiments conducted aboard the International Space Station (ISS). This study represents a culmination of recent efforts to predict ISS data using CFD methods. Key findings from the study are as follows:

(1) For all three mass velocities considered, $G = 199.9$, 799.9, and 2399.9 kg/m^2 s, the CFD model effectively captures increasing void fraction in response to increasing heat flux along the heated flow channel. In particular, for the two lower mass velocities, the CFD model shows good agreement with the high-speed video images acquired from the ISS experiments by accurately simulating interfacial behaviors and structures including bubble nucleation, growth, departure, and coalescence along the heated length for the two heat fluxes considered of around 20% and 60% CHF. Moreover, the CFD model is able to simulate nucleating bubbles in the liquid film surrounding the vapor core in the downstream region of the flow channel, which enables accurate prediction of heated wall temperatures.
(2) For the highest mass velocity of $G = 2399.9$ kg/m^2 s and two heat flux percentages, a limitation of the CFD model is identified which stems from underprediction of vapor void fraction.
(3) CFD simulations are a powerful tool for predicting transport parameters that are crucial to understanding boiling flow, such as axial profiles and cross-sectional profiles of void fraction, fluid velocity, and mixture temperature, which are not easily measurable in experiments.
(4) For each of the three mass velocities and two heat flux percentages considered, both measured and predicted wall temperatures are fairly uniform along the heated length, excepting slightly lower values in the entrance and exit regions. The upstream lower wall temperatures are attributed to the development of thermal boundary layer where ineffective single-phase heat transfer dominates thermal energy transport, whereas the downstream lower temperatures are the result of enhanced heat transfer coefficient induced by the flow acceleration with the increased vapor void fraction in the exit region.
(5) The present computational model predicts the axial variation of bulk fluid temperature and the heated wall temperature with fairly good accuracy. This validates the model's potential as a reliable alternative for designing practical two-phase thermal systems in space applications.

Declaration of Competing Interest

The authors declare the following financial interests/personal relationships which may be considered as potential competing interests:

Issam Mudawar reports financial support was provided by NASA. Issam Mudawar reports a relationship with NASA that includes: funding grants.

Data availability

Possibly at a future date following approvals

Acknowledgment

The authors are grateful for financial support provided by the National Aeronautics and Space Administration (NASA) under grant no. 80NSSC22K0328.

References

[1] I. Mudawar, Chapter five—Flow boiling and flow condensation in reduced gravity, Adv. Heat Transf. 49 (2017) 225–306.
[2] Y. Zhao, H. Hui Tan, B. Zhang, A high-resolution characteristics-based implicit dual time-stepping VOF method for free surface flow simulation on unstructured grids, J. Comput. Phys. 183 (2002) 233–273.
[3] S. Osher, J.A. Sethian, Fronts propagating with curvature-dependent speed: algorithms based on Hamilton–Jacobi formulations, J. Comput. Phys. 79 (1988) 12–49.
[4] C.W. Hirt, B.D. Nichols, Volume of fluid (VOF) method for the dynamics of free boundaries, J. Comput. Phys. 39 (1981) 201–225.
[5] A. Bourlioux, A coupled level-set volume-of-fluid algorithm for tracking material interfaces, in: Proc. 6th Int. Symp. Comput. Fluid Dyn, Lake Tahoe, CA, 1995.
[6] M. Sussman, E.G. Puckett, A coupled level set and volume-of-fluid method for computing 3D and axisymmetric incompressible two-phase flows, J. Comput. Phys. 162 (2000) 301–337.
[7] D. Gerlach, G. Tomar, G. Biswas, F. Durst, Comparison of volume-of-fluid methods for computing surface tension-dominant two-phase flows, Int. J. Heat Mass Transf. 49 (2006) 740–754.
[8] B.M. Ningegowda, B. Premachandran, A coupled level set and volume of fluid method with multi-directional advection algorithms for two-phase flows with and without phase change, Int. J. Heat Mass Transf. 79 (2014) 532–550.
[9] N. Balcázar, O. Lehmkuhl, L. Jofre, J. Rigola, A. Oliva, A coupled volume-of-fluid/level-set method for simulation of two-phase flows on unstructured meshes, Comput. Fluids 124 (2016) 12–29.
[10] V. Pandey, G. Biswas, A. Dalal, Saturated film boiling at various gravity levels under the influence of electrohydrodynamic forces, Phys. Fluids 29 (2017), 032104.
[11] D. Lorenzini, Y. Joshi, Comparison of the volume of fluid and CLSVOF methods for the assessment of flow boiling in silicon microgaps, J. Heat Transfer 139 (2017), 111506.
[12] D. Lorenzini, Y. Joshi, Numerical modeling and experimental validation of two-phase microfluidic cooling in silicon devices for vertical integration of microelectronics, Int. J. Heat Mass Transf. 138 (2019) 194–207.
[13] M. Bahreini, J.F. Derakhshandeh, A. Ramiar, E. Dabirian, Numerical study on multiple bubbles condensation in subcooled boiling flow based on CLSVOF method, Int. J. Therm. Sci. 170 (2021), 107121.
[14] S. Kim, J. Lee, J. Hartwig, I. Mudawar, Computational investigation of vertical upflow boiling of liquid nitrogen and effects of bubble collision dispersion force, Int. J. Heat Mass Transf. 203 (2023), 123780.
[15] Y.-Y. Hsu, R.W. Graham, An analytical and experimental study of the thermal boundary layer and ebullition cycle in nucleate boiling, NASA report, 1961.
[16] R. Jafari, T. Okutucu-Özyurt, Numerical simulation of flow boiling from an artificial cavity in a microchannel, Int. J. Heat Mass Transf. 97 (2016) 270–278.
[17] Y. Lin, Y. Luo, W. Li, W.J. Minkowycz, Enhancement of flow boiling heat transfer in microchannel using micro-fin and micro-cavity surfaces, Int. J. Heat Mass Transf. 179 (2021), 121739.
[18] Y.-J. Chen, K. Ling, H. Ding, Y. Wang, S.-Q. Jin, W.-Q. Tao, 3-D numerical study of subcooled flow boiling in a horizontal rectangular mini-channel by VOSET, Int. J. Heat Mass Transf. 183 (2022), 122218.
[19] S.C.P. Cheung, S. Vahaji, G.H. Yeoh, J.Y. Tu, Modeling subcooled flow boiling in vertical channels at low pressures – Part 1: Assessment of empirical correlations, Int. J. Heat Mass Transf. 75 (2014) 736–753.
[20] Y. Chen, Y. Zou, B. Yu, D. Sun, X. Chen, Effects of surface wettability on rapid boiling and bubble nucleation: A molecular dynamics study, Nanoscale Microscale Thermophys. Eng. 22 (2018) 198–212.
[21] Y. Chen, B. Yu, Y. Zou, B. Chen, W. Tao, Molecular dynamics studies of bubble nucleation on a grooved substrate, Int. J. Heat Mass Transf. 158 (2020), 119850.

[22] J. Lee, L.E. O'Neill, S. Lee, I. Mudawar, Experimental and computational investigation on two-phase flow and heat transfer of highly subcooled flow boiling in vertical upflow, Int. J. Heat Mass Transf. 136 (2019) 1199–1216.
[23] J. Lee, L.E. O'Neill, I. Mudawar, 3-D computational investigation and experimental validation of effect of shear-lift on two-phase flow and heat transfer characteristics of highly subcooled flow boiling in vertical upflow, Int. J. Heat Mass Transf. 150 (2020), 119291.
[24] J. Lee, L.E. O'Neill, I. Mudawar, Computational prediction of key heat transfer mechanisms and hydrodynamic characteristics of critical heat flux (CHF) in subcooled vertical upflow boiling, Int. J. Heat Mass Transf. 161 (2020), 120262.
[25] J. Lee, I. Mudawar, M.M. Hasan, H.K. Nahra, J.R. Mackey, Experimental and computational investigation of flow boiling in microgravity, Int. J. Heat Mass Transf. 183 (2022), 122237.
[26] J. Lee, S. Kim, I. Mudawar, Assessment of computational method for highly subcooled flow boiling in a horizontal channel with one-sided heating and improvement of bubble dispersion, Int. J. Therm. Sci. 184 (2023), 107963.
[27] I. Mudawar, V.S. Devahdhanush, S.J. Darges, M.M. Hasan, H.K. Nahra, R. Balasubramaniam, J.R. Mackey, Heat transfer and interfacial flow physics of microgravity flow boiling in single-side-heated rectangular channel with subcooled inlet conditions—Experiments onboard the international space station, Int. J. Heat Mass Transf. 207 (2023), 123998.
[28] E.W. Lemmon, M.L. Huber, M.O. McLinden, NIST standard reference database 23, Reference Fluid Thermodynamic and Transport Properties (REFPROP), Version 9, 2010.
[29] W.H. Lee, A pressure iteration scheme for two-phase flow modeling, Reactor Safety, Appl. 1 (1980) 407–431.
[30] J.U. Brackbill, D.B. Kothe, C. Zemach, A continuum method for modeling surface tension, J. Comput. Phys. 100 (1992) 335–354.
[31] K.K. So, X.Y. Hu, N.A. Adams, Anti-diffusion method for interface steepening in two-phase incompressible flow, J. Comput. Phys. 230 (2011) 5155–5177.
[32] ANSYS FLUENT, Theory Guide, ANSYS Inc., Canonburg, PA, 2009.
[33] R. Raj, C. Kunkelmann, P. Stephan, J. Plawsky, J. Kim, Contact line behavior for a highly wetting fluid under superheated conditions, Int. J. Heat Mass Transf. 55 (2012) 2664–2675.
[34] R. Mei, J.F. Klausner, Shear lift force on spherical bubbles, Int. J. Heat Fluid Flow 15 (1994) 62–65.
[35] S.L. Sharma, T. Hibiki, M. Ishii, C.S. Brooks, J.P. Schlegel, Y. Liu, J.R. Buchanan, Turbulence-induced bubble collision force modeling and validation in adiabatic two-phase flow using CFD, Nucl. Eng. Des. 312 (2017) 399–409.
[36] X. Sun, Two-Group Interfacial Area Transport Equation for a Confined Test Section, Purdue University, 2001.
[37] M. Ishii, N. Zuber, Drag coefficient and relative velocity in bubbly, droplet or particulate flows, AIChE J. 25 (1979) 843–855.
[38] I. Mudawar, J. Lee, Experimental and computational investigation into hydrodynamic and heat transfer characteristics of subcooled flow boiling on the International Space Station, Int. J. Heat Mass Transf. 207 (2023), 124000.
[39] Q. Li, D. Ming, M. Lei, X. Guo, J. Liu, H. Zhu, L. Fang, Z. Wang, Numerical investigation on the coupled mechanisms of bubble breakup in a venturi-type bubble generator, Eng. Appl. Comput. Fluid Mech. 16 (2022) 229–247.
[40] B.B. Mikic, W.M. Rohsenow, A new correlation of pool-boiling data including the effect of heating surface characteristics, J. Heat Transf. 91 (2) (1969) 245–250.
[41] N. Zuber (Ed.), Hydrodynamic aspects of boiling heat transfer (thesis), in Other Information: Orig. Receipt, Medium: ED, 1959, p. 210.
[42] M. Shah, A general correlation for heat transfer during subcooled boiling in pipes and annuli, ASHRAE Trans. 83 (1977) 202–217.
[43] C.R. Kharangate, I. Mudawar, M. Hasan, Photographic study and modeling of critical heat flux in horizontal flow boiling with inlet vapor void, Int. J. Heat Mass Transf. 55 (2012) 4154–4168.
[44] Y. Chen, S. Jin, B. Yu, K. Ling, D. Sun, W. Zhang, K. Jiao, W. Tao, Modeling and study of microlayer effects on flow boiling in a mini-channel, Int. J. Heat Mass Transf. 208 (2023), 124039.
[45] J. Lee, I. Mudawar, Fluid flow and heat transfer characteristics of low temperature two-phase micro-channel heat sinks—Part 2: subcooled boiling pressure drop and heat transfer, Int. J. Heat Mass Transf. 51 (2008) 4327–4341.
[46] L.E. O'Neill, I. Mudawar, Review of two-phase instabilities in macro- and micro-channel systems, Int. J. Heat Mass Transf. 157 (2020), 119738.